scientific reports

Check for updates

OPEN

Biosynthesis and characterization of iron oxide nanoparticles fabricated using cell-free supernatant of *Pseudomonas fluorescens* for antibacterial, antifungal, antioxidant, and photocatalytic applications

Sanaz Ashrafi-Saiedlou[1]✉, MirHassan Rasouli-Sadaghiani[1]✉, Mohammad Fattahi[2] & Youbert Ghosta[3]

This study investigates the biosynthesis of iron oxide nanoparticles (Fe_2O_3NPs) using the cell-free supernatant of *Pseudomonas fluorescens*. The synthesized Fe_2O_3NPs were characterized through UV–VIS, XRD, FTIR, FESEM, EDX, TEM, BET, and VSM analyses. The XRD results confirmed that Fe_2O_3NPs were successfully synthesized and EDX analysis indicated that iron accounted for 89.5% of the sample composition. Imaging via SEM and TEM revealed average diameters of 20.43 ± 5.38 nm and 24.32 ± 5.03 nm, respectively. The antimicrobial effects of Fe_2O_3NPs were assessed against four bacterial strains and four fungal species. Inhibition zones of 8.35 ± 0.103 mm and 8.31 ± 0.128 mm were observed for *Pseudomonas syringae* and *Staphylococcus aureus* at a concentration of 400 µg mL^{-1} of Fe_2O_3NPs. Antifungal efficacy showed growth rate reductions of 90.4% for *Aspergillus niger*, 71.1% for *Monilinia fructigena*, 68.8% for *Botrytis cinerea*, and 84.2% for *Penicillium expansum*, compared to controls. The nanoparticles demonstrated photocatalytic degradation efficiencies of 89.93%, 84.81%, and 79.71% for methyl violet, methyl orange, and methylene blue, respectively. Also Fe_2O_3NPs exhibited significant DPPH free radical scavenger activity with an IC_{50} value of 8.45 ± 0.59 µg mL^{-1}. The study's findings underscored the significant potential of Fe_2O_3NPs in addressing environmental pollution and combating pathogenic microorganisms.

Keywords Green synthesis, Iron oxide nanoparticles, *Pseudomonas fluorescens*, Photocatalytic degradation, Antimicrobial activity, Antioxidant activity, VSM, BET

Interest in nanoscale materials is rising because their smaller size increases surface area, significantly altering their properties[1]. This phenomenon can induce modifications in the electronic, optical, thermal, and chemical reactivity properties of compounds[2]. Generally, chemical, physical, and biological methods are commonly employed for nanoparticle production[3]. Chemical techniques for synthesizing nanoparticles include precipitation, oxidation or reduction, and reactions involving electron transfer. In contrast, physical methods use a bottom-up approach with two key stages: material evaporation followed by rapid, controlled condensation to produce nanoparticles of specific sizes. Green synthesis focuses on creating metallic and metal oxide nanoparticles through two main approaches: plant-mediated and microorganism-mediated biosynthesis[3].

The use of hazardous materials in conventional chemical methods for nanoparticle synthesis poses significant toxicity and environmental risks due to the persistent toxic byproducts. As a result, there is a growing

[1]Department of Soil Science, Faculty of Agriculture, Urmia University, Urmia, Iran. [2]Department of Horticulture, Faculty of Agriculture, Urmia University, Urmia, Iran. [3]Department of Plant Protection, Faculty of Agriculture, Urmia University, Urmia, Iran. ✉email: sanazashrafi92@yahoo.com; m.rsadaghiani@urmia.ac.ir

preference for alternative synthesis approaches[3,4]. Green nanotechnology minimizes the production of toxic chemicals, ensuring high environmental compatibility. The principles of green synthesis are crucial for reducing or eliminating hazardous compounds in the creation of synthetic and chemical products. The resulting green nanomaterials have significant potential for widespread applications across various industries[5,6].

In recent times, biological methodologies employing fungi, bacteria, and plant extracts have garnered considerable attention due to their inherent simplicity, cost-effectiveness, high efficiency, non-toxic nature, and environmental friendliness relative to conventional methods[7]. This shift towards biological approaches signifies a pivotal step towards sustainable and environmentally conscious nanomaterial synthesis[8].

Microorganisms are prominent in the green synthesis of nanoparticles because of their rapid growth, ease of cultivation, and adaptability to various environmental conditions, including temperature, pH, and pressure[9]. Various microorganisms serve as potential biological catalysts for producing environmentally friendly and cost-effective nanoparticles comprising metals like silver, gold, iron, copper, zinc, titanium, palladium, and nickel. The biosynthetic process of nanoparticles in microorganisms involves capturing specific metal ions from the surroundings and enzymatically converting them into elemental form, followed by a reduction mechanism[10].

Not all microorganisms can synthesize nanoparticles, as this ability depends on specific metabolic pathways and enzymes. Intracellular nanoparticle biosynthesis involves specialized transport systems, with the negatively charged cell wall facilitating the deposition of positively charged metal ions through electrostatic interactions. Extracellular nanoparticle synthesis is driven by nitrate reductase, an enzyme found either in the cell wall or secreted into the growth medium, proteins, and other biological molecules within microorganisms which reduces metal ions and aids in nanoparticle production[11,12]. Proteins secreted by microorganisms primarily act as stabilizing agents, ensuring colloidal stability and preventing nanoparticle aggregation[11].

Research indicates that NADH-dependent enzymes are responsible for the synthesis of nanoparticles, with reduction mechanisms being initiated by electron transfer from NADH through NADH-dependent reductases acting as electron carriers[13]. Various bacteria, such as *Pseudomonas aeruginosa*, *Visella oriza*, *Bacillus methylotrophicus*, *Bhargavaea indica*, *Lactobacillus*, *Enterobacter*, *Corynebacterium*, *Rhodobacter*, *Brevibacterium*, and *Brevibacterium frigoritolerans*, have been shown to possess the capability to synthesize different types of nanoparticles[14–17].

Nanotechnology is rapidly expanding today, with diverse applications across physical, chemical, and biological sciences[1]. One specific class of nanoparticles, metal oxide nanoparticles ranging from 1 to 100 nm, has unique physical and chemical properties. These nanoparticles are particularly useful as catalysts and antimicrobial agents[18,19].

Industries like textiles, food processing, cosmetics, pharmaceuticals, leather production, and paper manufacturing generate colored effluents, including methylene blue, Congo red, methyl orange, methyl red, naphthol orange, acid orange, and rhodamine B. This highlights the importance of addressing organic colorants as significant environmental pollutants. Various methods have been employed for colorant removal from industrial wastewater, including surface adsorption, membrane processes, biological treatments, and advanced oxidation processes[20]. Photocatalytic processes have been a longstanding environmental solution in industrialized nations and continue to evolve with the introduction of new photocatalytic materials that offer diverse properties[21]. The Nano material properties are closely linked to its size and shape. By manipulating the structure's dimensions and morphology, novel materials with unique characteristics can be developed[22]. Iron oxide nanoparticles are essential in industrial microbiology, stabilizing microbial cells in processes like wastewater treatment and eliminating microbial contaminants. Nanostructured iron oxide photocatalysts have a high surface-to-volume ratio, making them a key technology for controlling environmental pollution[23].

The overuse of antibiotics has led to bacterial resistance, prompting researchers to seek alternative solutions. Metallic oxide nanoparticles, such as iron oxides, zinc oxide, and titanium dioxide, have emerged as promising candidates due to their broad spectrum of toxic and cell-killing properties against various microorganisms, including bacteria, fungi, and viruses[24]. Among these, iron oxide nanoparticles have garnered significant attention from the scientific community because of their advantageous magnetic properties, high biocompatibility, low toxicity, and superior efficacy compared to other types of nanoparticles. In addition several studies have reported on the antimicrobial effects of iron oxide nanoparticles against both gram-positive and gram-negative bacteria, as well as fungi[24–26]. The predominant proposed mechanism underlying the antimicrobial properties of metallic oxide nanoparticles involves disrupting the cell wall and causing damage to enzymes and nucleic acids[27,28]. These nanoparticles have proven effective as photocatalysts for degrading organic pollutants in wastewater and air, providing a sustainable approach to environmental cleanup[29,30]. Iron oxide nanoparticles are promising for biomedical applications, particularly in drug delivery, imaging, and developing innovative antimicrobial agents due to their antioxidant and antimicrobial properties, which may lead to novel therapies for oxidative stress-related diseases and enhance healthcare and food safety[25,28,31]. The significance of green synthesis methods for nanoparticle production lies in their ability to create environmentally friendly and sustainable products, aligning with green chemistry principles and advancing eco-friendly nanotechnologies. In the present study, the cell-free supernatant of *Pseudomonas fluorescens* was utilized for the green synthesis of iron nanoparticles. It is expected that the iron nanoparticles synthesized from this bacterium will demonstrate multifunctional properties, including antioxidant, antibacterial, antifungal, and photocatalytic activities. Therefore the main objectives of this research are as follows: (I) To perform the green synthesis of Fe_2O_3NPs using the cell-free supernatant of *Pseudomonas fluorescens*; (II) To characterize the synthesized nanoparticles through various techniques, including field emission scanning electron microscopy (FESEM), Fourier-transform infrared spectroscopy (FTIR), UV–Visible spectroscopy (UV–Vis), X-ray diffraction (XRD), energy-dispersive X-ray spectroscopy (EDX), transmission electron microscopy (TEM), Brunauer–Emmett–Teller (BET) analysis, and vibrating sample magnetometer (VSM); (III) To evaluate the antibacterial and antifungal activity, DPPH free radical scavenging activity, and photocatalytic properties of the synthesized nanoparticles.

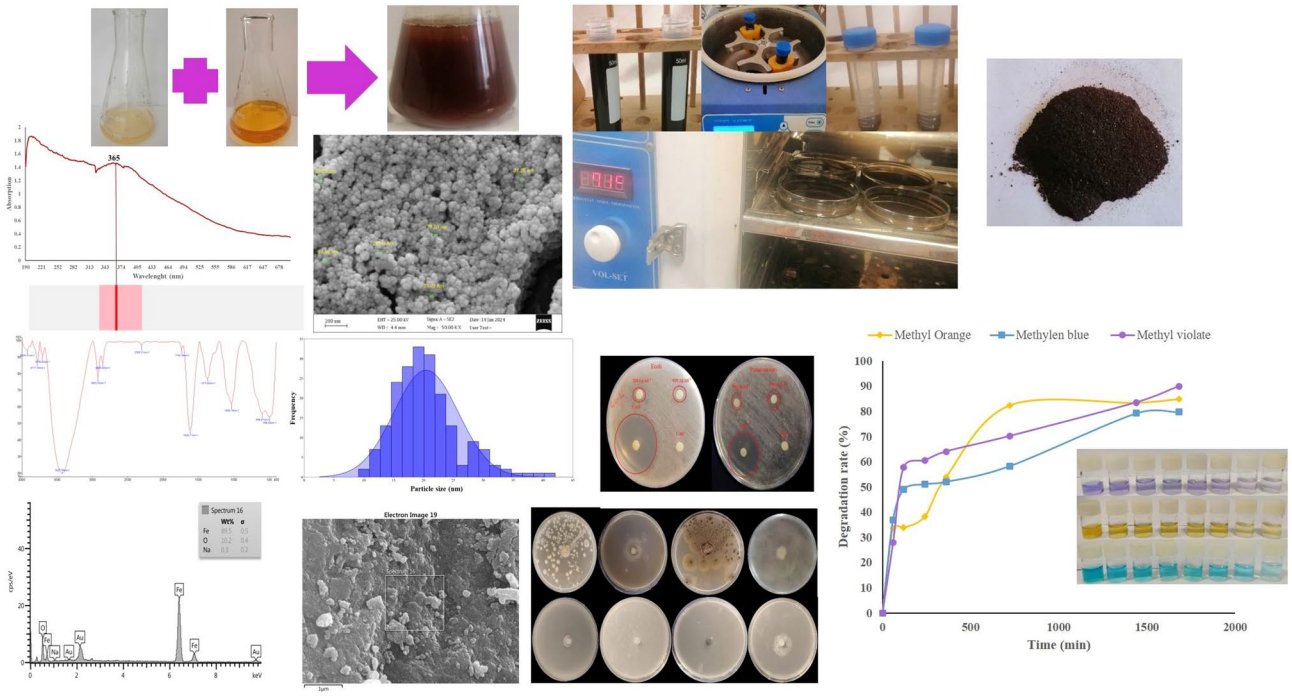

Fig. 1. Schematic overview of green synthesis process, characterization, and experimental procedures.

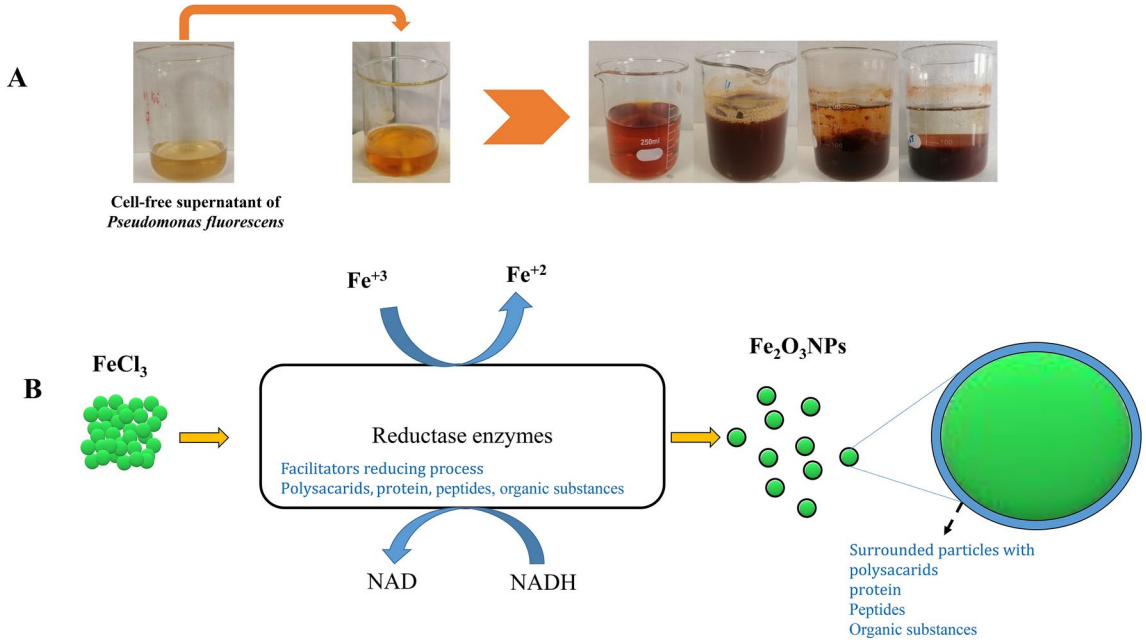

Fig. 2. (**A**) Color changing during synthesis of Fe_2O_3NPs; (**B**) Synthesis mechanism of Fe_2O_3NPs.

Results and discussion

Characterization of Fe_2O_3NPs

The green synthesis of Fe_2O_3NPs was accomplished using *Pseudomonas fluorescens* as the selected model microorganism. Schematic overview of green synthesis process, characterization, and experimental procedures conducted in this study is shown in Fig. 1. The synthesis procedure involved the addition of 0.1 M $FeCl_3.6H_2O$ to the cell-free supernatant of *Pseudomonas fluorescens*, resulting in a visible color shift from yellow to dark reddish brown, as depicted in Fig. 2A. The observed color change provides clear evidence of the significant reduction capacity exhibited by the supernatant of *Pseudomonas fluorescens*, which consequently results in the formation of iron-based nanoparticles. Previous studies have demonstrated that microorganisms exhibit

the capability to reduce metal ions by employing a diverse array of enzymes[11,13,32,33]. In addition to enzymes, extracellular polysaccharides, proteins, peptides, cofactors, and other organic compounds play pivotal roles in the biosynthesis process, functioning as essential stabilizing, capping, and reducing agents[7]. The production of metal nanoparticles by microorganisms plays a crucial role in alleviating the detrimental effects of metal ions present in the microbial growth environment. Through biological reduction processes, microorganisms enzymatically transform toxic metal ions into less harmful metal species using reductase and/or nitrate reductase enzymes, along with specific NADH assistance. Moreover, the presence of certain polysaccharides and organic compounds, generated by microorganisms both intracellularly and in the growth medium, facilitates the generation of metal nanoparticles. These organic substances contain functional groups such as cysteine, histidine, aldehydes, and ketones, which are influential in the reduction of metal ions to yield metal nanoparticles[11,13,32]. A schematic representation illustrating the green synthesis mechanism of Fe_2O_3NPs is depicted in Fig. 2B. To effectively characterize the synthesized nanoparticles, a variety of analytical techniques including UV–vis spectroscopy, XRD, FTIR, FESEM, EDX, TEM, BET, and VSM were utilized.

UV–visible spectroscopy

The analysis of UV–vis spectra, commonly conducted in the wavelength span of 190–700 nm, plays a vital role in the identification of substances. Figure 3A displays the UV–vis spectra of the synthesized Fe_2O_3NPs. The synthesis of Fe_2O_3NPs is typically associated with a wavelength range of 320–420 nm[34]. Hence, the peak observed at 365 nm was ascribed to the surface plasmon resonance of iron nanoparticles.

XRD analysis

XRD is a versatile analytical technique that is widely used for the structural analysis of materials, including magnetic nanoparticles[35]. In the current study, XRD was employed to examine the structural attributes of the fabricated Fe_2O_3NPs. The XRD assessment conducted in this research revealed prominent diffraction patterns at distinct 2θ values spanning from 20 to 80 degrees. Prominent peaks were detected at angular positions of 24.13°, 33.15°, 35.61°, 40.85°, 49.48°, 54.09°, 62.45° and 63.99°, corresponding to specific crystallographic planes indexed as (012), (104), (110), (113), (024), (116), (214) and (300) respectively (JCPDS card no: 00–033-0664) (Fig. 3B). Furthermore, the material was confirmed to exhibit an rhombohedral crystal system[36]. The discerned peaks in the XRD analysis signify the successful synthesis of Fe_2O_3NPs utilizing the cell-free supernatant of *Pseudomonas fluorescens*, a process that facilitated the conversion of iron ions into iron atoms. The crystal size of the synthesized Fe_2O_3NPs, derived from Scherrer's equation, was measured to be 22.73 nm.

FTIR spectroscopy

The FTIR spectroscopy analysis of the synthesized Fe_2O_3NPs exhibited distinct spectral peaks across the range of 4000 to 400 cm^{-1}, indicative of specific functional groups likely derived from compounds present in the bacterial cell-free supernatant utilized during the synthesis process. Notable peaks were observed at 3924.41 cm^{-1}, 3777.44 cm^{-1}, 3708.62 cm^{-1}, 3427.69 cm^{-1}, 2923.43 cm^{-1}, 2855.9 cm^{-1}, 2305.31 cm^{-1}, 1740.36 cm^{-1}, 1620.71 cm^{-1}, 1373.62 cm^{-1}, 1036.78 cm^{-1}, 595.67 cm^{-1}, and 495.04 cm^{-1} (Fig. 3C).

The spectral bands within the range of 3400–4000 cm^{-1} can be attributed to the stretching vibrations of hydroxyl (OH) and amine (NH) functional groups commonly found in phenolic, alcoholic, or amino compounds present in the bacterial cell-free supernatant[37]. These functional groups play a critical role in stabilizing nanoparticles by forming hydrogen bonds or electrostatic interactions with nanoparticle surfaces, thereby reducing agglomeration and enhancing the dispersion of Fe_2O_3NPs in the solution[38–40]. Conversely, the region spanning 2800–3000 cm^{-1} corresponds to the stretching vibrations of CH groups in alkenes[41], which may contribute to stabilization by establishing a steric barrier around the nanoparticles, thus preventing further aggregation[39]. Moreover, the spectral range of 2000–2400 cm^{-1} indicates the presence of triple bond linkages between carbon–carbon (CC) and carbon–nitrogen (CN) bonds[42], suggesting the involvement of functionalized organic moieties that may enhance binding affinity toward iron ions, facilitating their interaction during nanoparticle formation[39,40]. The spectral wavelengths between 1600–1800 cm^{-1} signify the presence of carboxylic acid (C–O) and amide (C=O) groups in proteins[41,43], which can stabilize nanoparticles through coordination chemistry, allowing these groups to form direct chemical bonds with the iron oxide surface. Furthermore, the spectral features within the range of 1300–1400 cm^{-1} are indicative of methyl (CH_3) functional groups[44,45], further supporting the hypothesis that organic molecules significantly contribute to the coating and stabilization of the nanoparticles[38,46]. The region of 1000–1200 cm^{-1} is associated with the C–O–C functional group[47], suggesting the presence of ether functionalities that may further enhance the structural integrity of the nanoparticle coating. Finally, the spectral range of 496.04–596.67 cm^{-1} provides evidence of bond formation between iron and oxygen within the analyzed nanoparticles[44]. The establishment of these iron-oxygen bonds is crucial for the structural framework of Fe_2O_3NPs, reinforcing the stability imparted by the aforementioned organic functional groups[48].

The functional groups identified in our FTIR analysis highlight their potential roles in stabilizing the synthesized Fe_2O_3NPs. The stabilization mechanisms are attributed not only to steric hindrance and electrostatic interactions but also to specific chemical bonding between the functional groups and the nanoparticle surfaces. These interactions likely play a significant role in the overall synthesis process, promoting the formation and stability of Fe_2O_3NPs in the medium during synthesis[38,39,46,48].

SEM–EDX analysis

SEM and EDX are fundamental analytical techniques widely employed across various scientific disciplines, particularly in materials science research. SEM functions as a high-resolution imaging method, utilizing an electron beam to scan a sample's surface and generate detailed images that reveal the sample's topography. This

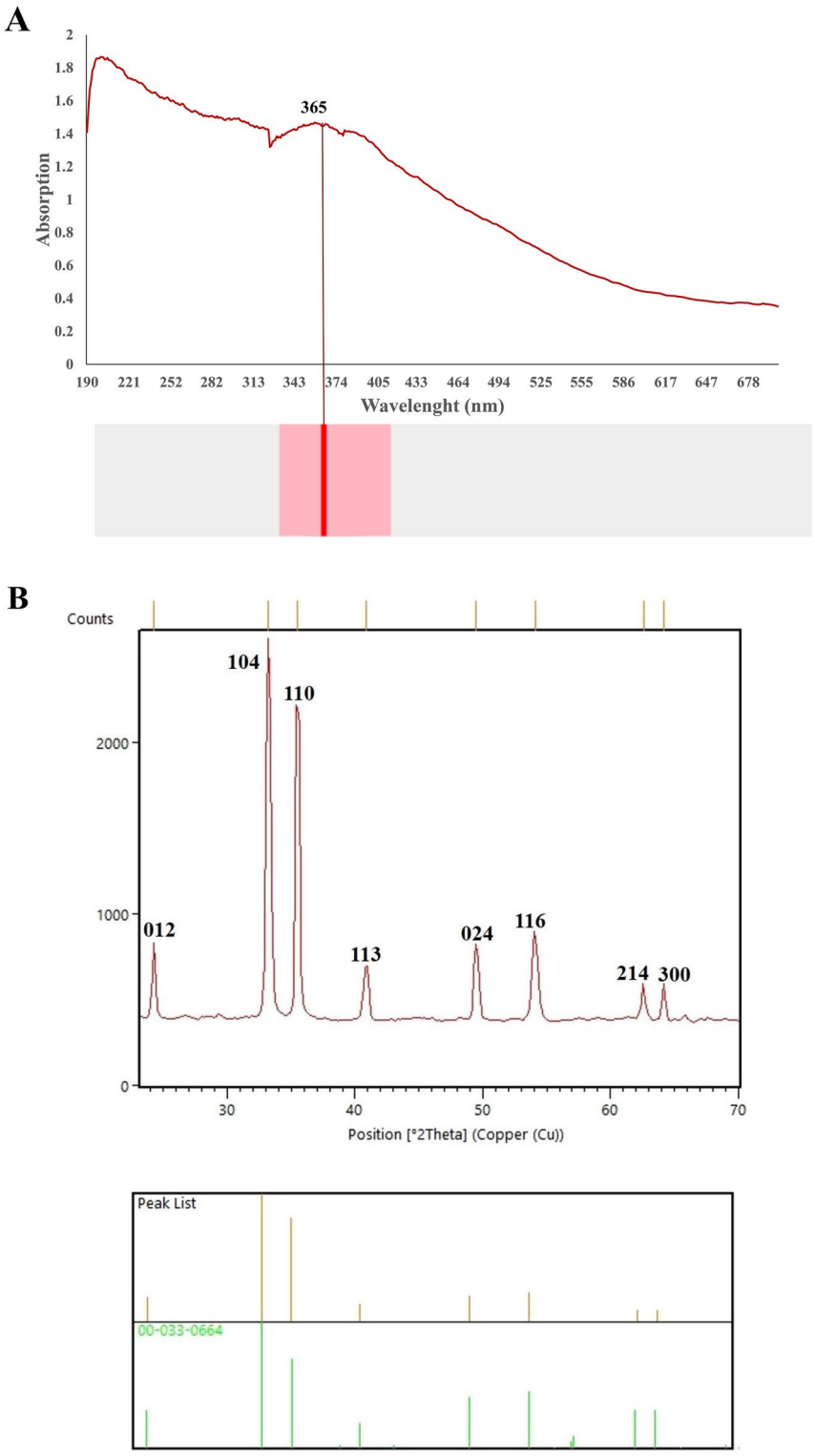

Fig. 3. Synthesized Fe_2O_3NPs characterization, (**A**) UV–Visible spectra of *Pseudomonas fluorescens* cell-free supernatant, (**B**) XRD pattern, (**C**) FTIR spectroscopy, (**D**) SEM image, (**E**) Size distribution histograms of Fe_2O_3NPs derived from SEM images data, (**F**) EDX analysis, (**G**) TEM image, (**H**) Size distribution histograms of Fe_2O_3NPs derived from TEM images data, (**I**) N_2 adsorption/desorption isotherms, (**J**) BJH pore size distributions plot of Fe_2O_3NPs, (**K**) VSM analysis.

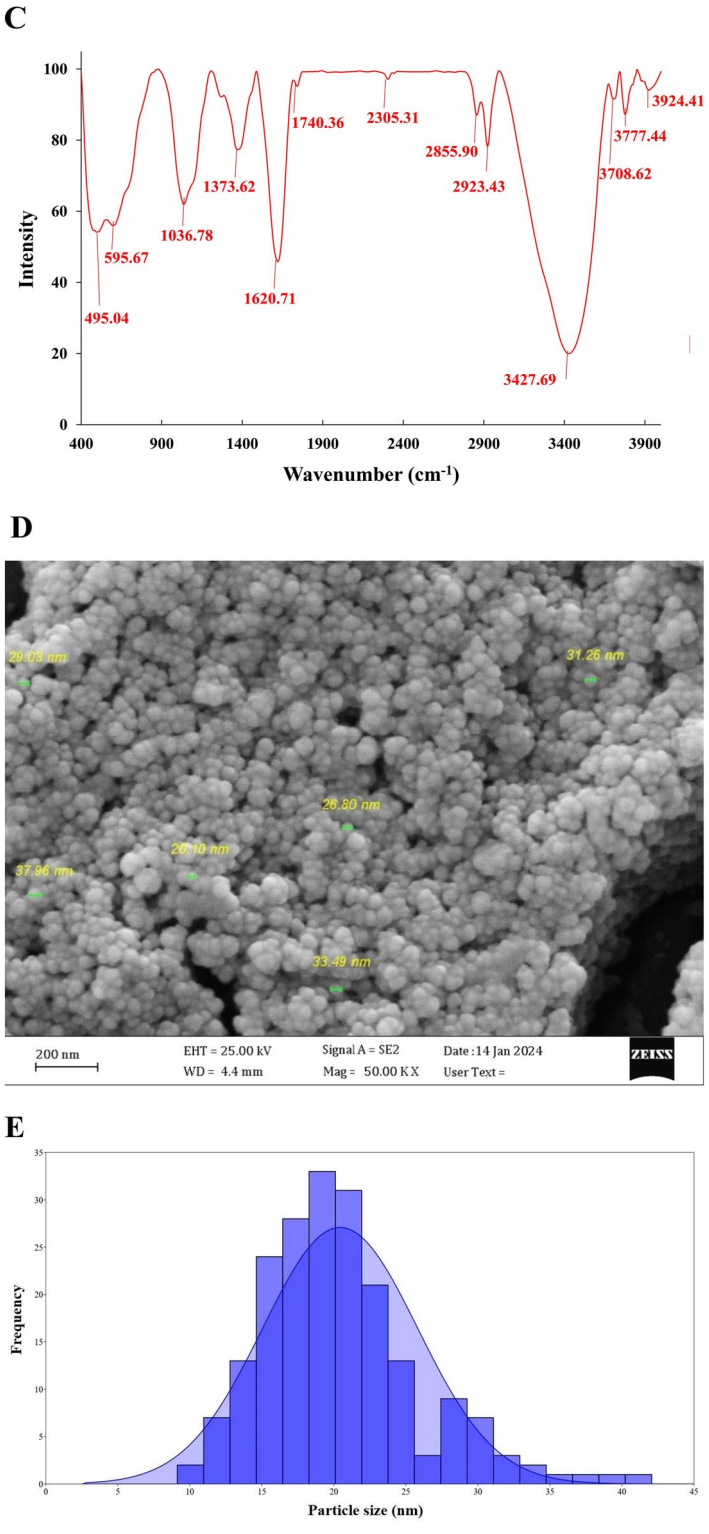

Figure 3. (continued)

technique enables the examination of a material's surface at high magnification levels, offering valuable insights into its structure, morphology, and composition. On the other hand, EDX is utilized for elemental analysis, utilizing the X-rays emitted by a sample when bombarded with electrons to identify and quantify the elements present. The combined use of SEM and EDX provides essential data on the properties and characteristics of diverse materials, making them indispensable tools in scientific investigations[49]. The SEM images depicted the presence of spherical nanoparticles with smooth surfaces (Fig. 3D). The size distribution assessment revealed that the average size of the synthesized nanoparticles was 20.43 ± 5.38 nm, as detailed in Table 1. Notably, particles

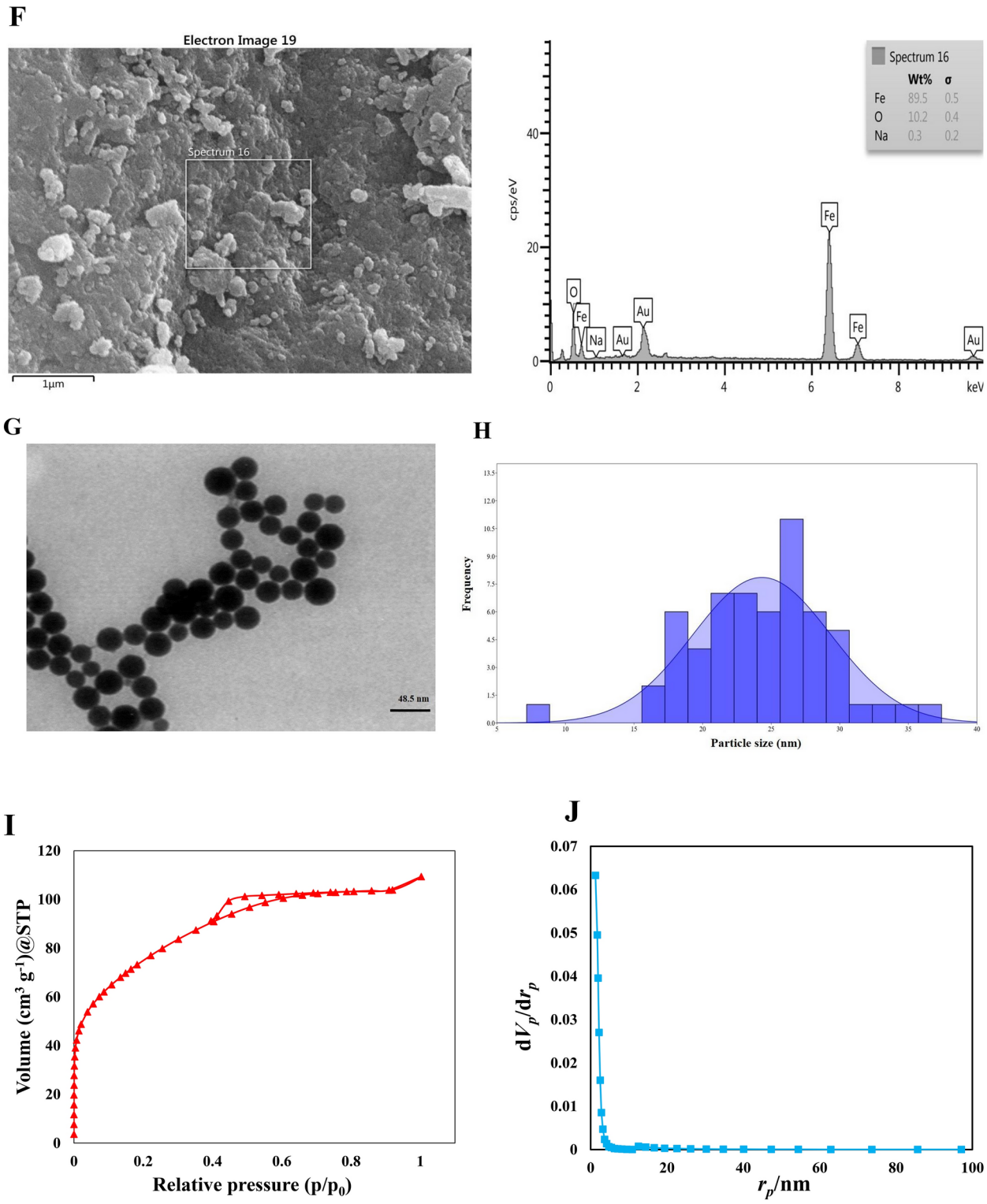

Figure 3. (continued)

within the 18–20 nm diameter range constituted a higher percentage (16.5%) in the particle size distribution plot, illustrated in Fig. 3E. Furthermore, EDX analysis of the synthesized Fe_2O_3NPs exhibited iron absorption peaks at 0.7, 6.4, and 7 keV, collectively constituting 89.5% of the sample composition. Additional absorptions were observed at 0.5 and 1 keV, corresponding to oxygen (10.2%) and sodium (0.3%) content, respectively (Fig. 3F).

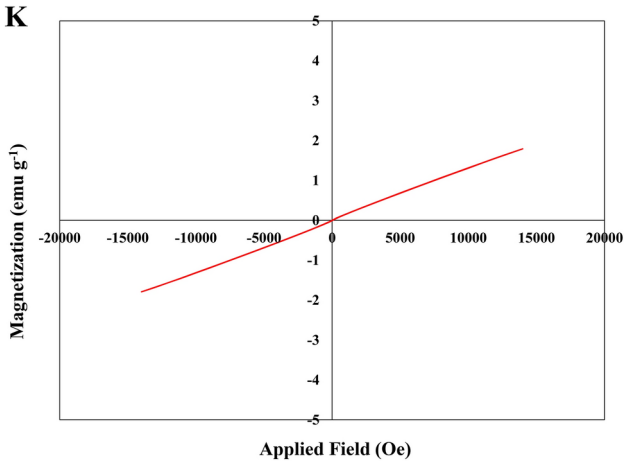

Figure 3. (continued)

Size distribution (nm)	Frequency (%)
9.12 – 10.95	1
10.95 – 12.78	3.5
12.78 – 14.61	6.5
14.61 – 16.44	12
16.44 – 18.27	14
18.27 – 20.10	16.5
20.10 – 21.93	15.5
21.93 – 23.76	10.5
23.76 – 25.59	6.5
25.59 – 27.42	1.5
27.42 – 29.25	4.5
29.25 – 31.08	3.5
31.08 – 32.91	1.5
32.91 – 34.74	1
34.74 – 36.56	0.5
36.56 – 38.39	0.5
38.39 – 40.22	0.5
40.22 – 42.05	0.5

Table 1. Size distribution of Fe_2O_3NPs determined using SEM images data.

TEM analysis

TEM is a powerful tool for evaluating nanoparticles at the nanoscale. This technique enables researchers to obtain high-resolution images of the internal structure and morphology of nanoparticles by directing an electron beam through a thin specimen. TEM allows for detailed analysis of particle size, shape, and distribution with precision at resolutions of a few angstroms. Such detailed examinations provide valuable insights into the physical characteristics of nanoparticles, aiding in their comprehensive characterization and advancing knowledge of their properties for applications in nanotechnology and materials science[49]. TEM image depicted in Fig. 3G showcases the synthesized Fe_2O_3NPs characterized by a consistent size distribution and a spherical structure. Through the utilization of Image J software, the diameters of the nanoparticles were carefully examined by converting the pixel measurements taken from the TEM images into nanometers following image calibration. The comprehensive analysis definitively verified that the synthesized Fe_2O_3NPs fell within the nanoscale category, displaying dimensions ranging from 7 to 37 nm, with an average diameter of 24.32 ± 5.03 nm (Table 2). The examination of the size distribution revealed that particles measuring between 25 and 27 nm demonstrated a significant presence, accounting for 18.64% of the particle size distribution histogram (Fig. 3H).

BET analysis

Figure 3I displays the nitrogen (N_2) adsorption and desorption isotherms for Fe_2O_3NPs. According to IUPAC classification, the observed adsorption–desorption curves are characteristic of a Type I isotherm with a Type H4 hysteresis loop. The reversible Type I isotherm is concave to the p/p° axis, with the adsorption approach

Size distribution (nm)	Frequency (%)
7.16—8.84	1.69
15.57 – 17.25	3.38
17.25 – 18.93	10.16
18.93 – 20.61	6.77
20.61 – 22.29	11.86
22.29 -23.97	11.86
23.97 -25.65	10.16
25.65 – 27.33	18.64
27.33 – 29.05	10.16
29.01 – 30.69	8.47
30.69 – 32.37	1.69
32.37 – 34.05	1.69
34.05 – 35.73	1.69
35.73 -37.41	1.69

Table 2. Size distribution of Fe_2O_3NPs determined using TEM images data.

to a limiting value as p/p° approaches 1. Such Type I isotherms are typical of microporous solids that exhibit relatively small external surface areas, including materials like activated carbons, molecular sieve zeolites, and certain porous oxides. Here, the limiting uptake is dictated by the volume of accessible micropores rather than by the internal surface area. The presence of the Type H4 hysteresis loop is often associated with narrow, slit-like pores. However, in this instance, the Type I isotherm suggests the presence of microporosity[50,51]. The pore size distributions of the samples were analyzed using the Barrett, Joyner, and Halenda (BJH) method, as illustrated in Fig. 3J The results from the BET and BJH analyses indicate that the mesoporous Fe_2O_3NPs have a BET specific surface area of 271.4 $m^2 g^{-1}$, an average pore diameter of 2.47 nm, and a BJH pore volume of 0.0952 $cm^3 g^{-1}$. Following the IUPAC nomenclature, nanopores can be classified into three categories: micropores (pore sizes < 2 nm), mesopores (2 nm < pore sizes < 50 nm), and macropores (pore sizes > 50 nm). Given the average pore diameter of 2.47 nm observed in this study, the Fe_2O_3NPs can be classified as mesoporous, with values very close to the micropores range[52].

VSM analysis

VSM apparatus are employed for the assessment of the magnetic characteristics of substances relative to magnetic field intensity, temperature variations, and temporal factors. These systems are optimally designed for applications in research and development, as well as for conducting production assessments, ensuring quality standards, and facilitating process monitoring[35] The examination of VSM test outcomes indicated that Fe_2O_3NPs, fabricated utilizing cell-free supernatant from *Pseudomonas fluorescens*, showcased the maximum saturated magnetization, measuring 1.79214 emu g^{-1}. Moreover, these nanoparticles demonstrated the most elevated hysteresis values, suggesting superior magnetic characteristics. Graph analysis depicted that subsequent to the cessation of the external magnetic field, the nanoparticles sustained their magnetic attributes, verifying a cohesive alignment between forward and reverse currents (Fig. 3K).

Antibacterial assays

The antimicrobial efficacy of Fe_2O_3NPs derived from *Pseudomonas fluorescens* was assessed against *S. enterica*, *E. coli*, and *S. aureus*, which are recognized as significant human pathogens. These microorganisms are commonly associated with food and medical contexts, representing notable risks for food poisoning and various infections[53–55]. *E. coli* is primarily linked to gastrointestinal infections, while *S. aureus* is associated with a range of skin infections. Additionally, *S. enterica* is a major contributor to foodborne illnesses. Testing our Fe_2O_3NPs against these strains underscores their potential for therapeutic applications in treating clinically relevant infections. Furthermore, we included *P. syringae*, a well-known plant pathogen capable of epiphytic growth on various plants[56], to assess the antimicrobial efficacy of our nanoparticles for using in agricultural contexts. This approach allows us to assess the effectiveness of Fe_2O_3NPs in enhancing crop disease management, thereby demonstrating the broader applicability of these nanoparticles.

Following a 24 h incubation period, the synthesized Fe_2O_3NPs demonstrated significant antimicrobial activity against all tested microbial pathogens, with efficacy varying among species ($P < 0.05$) (Table 3). The presence of Fe_2O_3NPs resulted in distinct zones of inhibition, indicating effective suppression of bacterial growth. The size of these inhibition zones varied with nanoparticle concentration, establishing a dose-dependent relationship[57,58] (Fig. 4A–D). Notably, the smallest inhibition zone was observed at a concentration of 200 µg mL^{-1}, while a concentration of 400 µg mL^{-1} exhibited enhanced antibacterial efficacy across all tested bacteria compared to the negative control. Specifically, *P. syringae* and *S. aureus* showed substantial growth suppression, with inhibition zone diameters of 8.35 ± 0.103 mm and 8.31 ± 0.128 mm, respectively, at the 400 µg mL^{-1} concentration (Fig. 4E). In contrast, *E. coli* exhibited the least inhibition zone (6.31 ± 0.112 mm). The variations in inhibition zone sizes among bacterial species can be attributed to differences in cell membrane structure[59]. The antibacterial effectiveness of metal oxide nanoparticles is influenced by factors such as concentration, size, distribution, and

Parameters	df	Mean Square (MS)	F—Value	Parameters	df	Mean Square (MS)	F—Value
FeNPs treatments (A)	3	2058.482*	9770.9870	FeNPs treatments (A)	3	35.612*	2559.2045
Bacteria (B)	3	4.538*	21.5419	Fungi (B)	5	47.692*	3427.2834
A × B	9	6.877*	32.6432	A × B	15	3.012*	216.4332
Error	32	0.211	–	Error	48	0.014	–
Coefficient of variation (%)	–	4.04	–	Coefficient of variation (%)	–	3.06	–

Table 3. Analysis of variance (ANOVA) for the Fe_2O_3NPs antibacterial and antifungal activities. * represents significance at $P \leq 0.05$.

agglomeration. Higher concentrations of nanoparticle suspensions can enhance antibacterial activity due to increased specific surface area[57,60,61]. Additionally, the susceptibility of bacteria to oxide nanoparticles is affected by synthesis parameters, bacterial cell wall structure, and interactions with bacterial cells[62]. The small size and high surface area-to-volume ratio of synthesized nanoparticles facilitate improved contact with microbial cells, enhancing their ability to penetrate membrane barriers and disrupt physiological functions[40,63]. Research indicates that the negatively charged components of bacterial membranes, such as amino acids and phosphates, attract the slightly positively charged Fe_2O_3NPs, promoting their attachment and internalization. Once inside the cell, Fe_2O_3NPs compromise plasma membrane integrity, leading to the depletion of intracellular ATP and disruption of cellular respiration. Furthermore, interactions between Fe_2O_3NPs with DNA and lipids, can impair cellular nucleic acids and proteins, ultimately resulting in cell death[40,64].

Fig. 4F illustrates the primary mechanisms of bacterial damage induced by Fe_2O_3NPs. These nanoparticles, as antimicrobial agents, exhibit diverse modes of action, often operating concurrently. Studies have shown that iron oxide nanoparticles can trigger various cellular responses, including the release of lactate dehydrogenase from cell membranes, chromosome condensation, and the production of reactive oxygen species (ROS) such as hydroxyl radicals, superoxide anions, hydrogen peroxide, and singlet oxygen[40,57]. These reactive species disrupt respiratory chains and disturb the balance between oxidative stress and the cellular antioxidant defense system, leading to lipid peroxidation, enzyme oxidation, DNA damage, and ultimately, cellular death[65,66]. Additionally, nanoparticles can interfere with the development of microfilaments and the cellular actin network, resulting in altered cellular morphology[63].

Iron oxide nanoparticles have also been observed to oxidize cell membranes, produce surface bubbles, and disrupt plasma membrane selectivity. The level of cellular toxicity varies across different organisms. Overall, the antimicrobial mechanisms of Fe_2O_3NPs derived from *P. fluorescens* include cellular membrane damage, ribosomal disassembly, enzyme inactivation, protein denaturation, and disruption of the electron transport chain. The interplay of nanoparticle size and electrostatic interactions leads to significant alterations in microbial physiological properties, impairing permeability and respiration. Variations in cell wall composition and thickness among microbial species may account for the observed discrepancies in inhibition zones. These findings underscore the potential of synthesized Fe_2O_3NPs as effective antimicrobial agents against multidrug-resistant pathogens due to their favorable physicochemical properties and modes of action.

Antifungal assays

The fungi *A. niger*, *M. fructigena*, *B. cinerea*, and *P. expansum,* which are economically significant pathogens associated with food spoilage and crop diseases[67,68], were selected as model organisms to investigate the antifungal activities of synthesized Fe_2O_3NPs. This selection allows for a comprehensive evaluation of the antifungal properties of Fe_2O_3NPs, particularly for their application in agricultural and food preservation settings. The analysis of variance demonstrated a significant influence of varying concentrations of Fe_2O_3NPs on the growth rate of fungi ($P \leq 0.05$), as outlined in Table 3. With increasing nanoparticle concentrations, there was a corresponding rise in the inhibitory impact on fungal growth (Fig. 5A–D). The control treatments displayed the highest growth rate at the end of the experiment (day 4), while the lowest growth rate, indicating the most significant inhibition, was linked to a concentration of 1000 µg mL^{-1} of Fe_2O_3NPs. Consequently, the growth rates of *A. niger*, *M. fructigena*, *B. cinerea*, and *P. expansum* decreased by 90.4%, 71.1%, 68.8%, and 84.2%, respectively, in comparison to the control treatments (Fig. 5E). Research has highlighted the potential for membrane impairment arising from direct or electrostatic interactions between Fe_2O_3NPs and cell surfaces, internalization of nanoparticles within cells, and the generation of ROS like H_2O_2 attributable to metal oxides. Fe_2O_3NPs exhibit an elevated surface-to-volume ratio, which enables robust adherence to the fungal cell surface and facilitates direct penetration into the cell to disrupt the cell wall[57]. The deactivation of fungi by Fe_2O_3NPs involves a direct engagement with cell surfaces, inducing changes in membrane permeability that trigger oxidative stress within fungal cells. This stress hinders cell proliferation, culminating in cellular death. Mechanisms underlying the infliction of damage to fungal cells include the initiation of ROS, instigating lipid peroxidation, adsorption embedment resulting in cell wall and membrane rupture, formation of pits and pores, leakage of DNA and organelles, ion liberation, DNA intercalation causing condensation and fragmentation, alterations in gene expression, release of cytochrome C from mitochondria prompting apoptosis, depolymerization of ribosomes, and binding to extracellular polymeric substances to impede biofilm formation[28,57,69]. Figure 5F illustrates the main ways in which fungal cells are harmed when exposed to Fe_2O_3NPs.

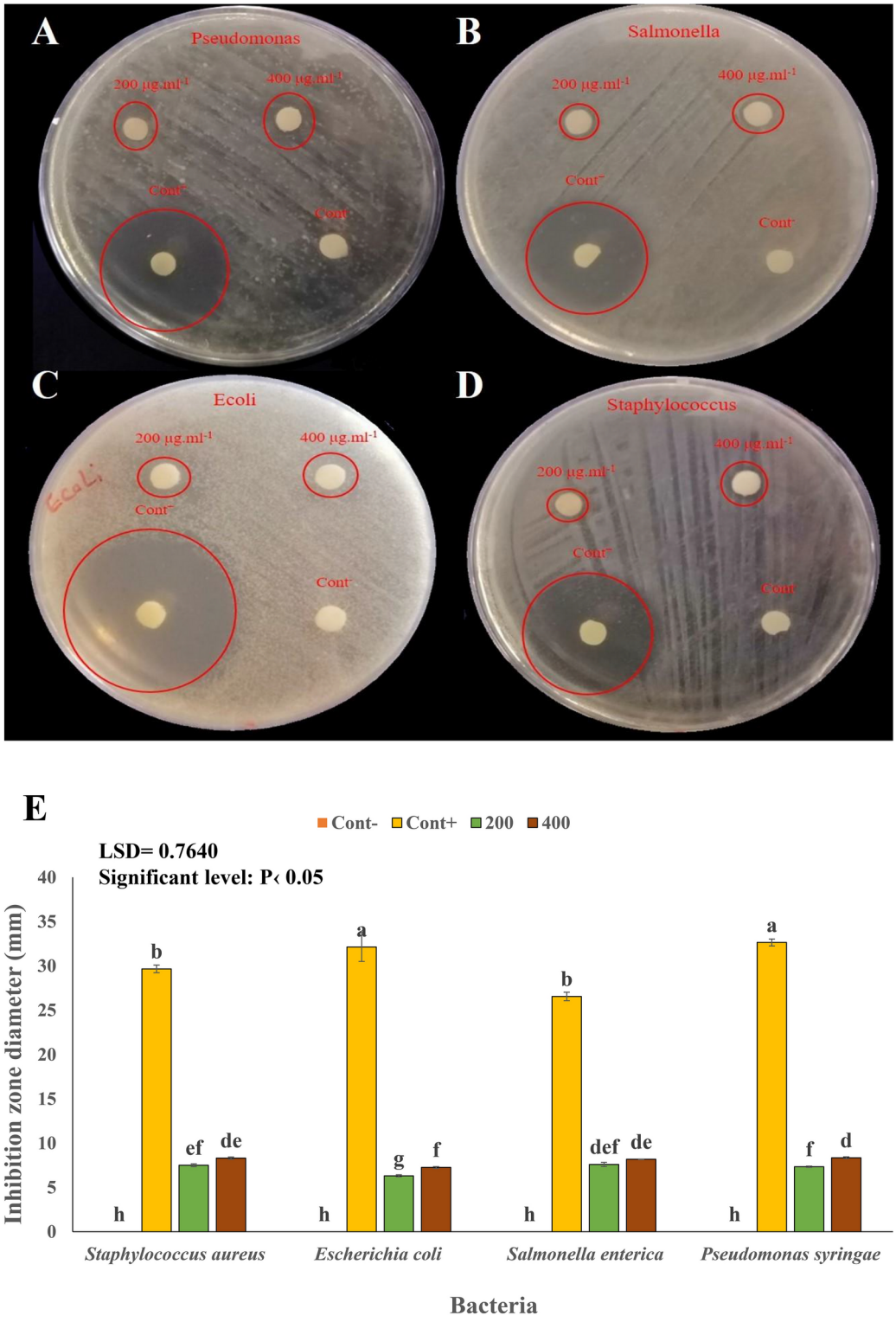

Fig. 4. Antibacterial activity of Fe_2O_3NPs against, (**A**) *Pseudomonas syringae*, (**B**) *Salmonella enterica*, (**C**) *Escherichia coli*, (**D**) *Staphylococcus aureus*; (**E**) Fe_2O_3NPs different concentrations impact on studied bacteria; (**F**) Antibacterial mechanism of Fe_2O_3NPs.

Dye degradation (photocatalytic activity)

The photocatalytic activity of the synthesized Fe_2O_3NPs was evaluated by investigating the degradation of methyl violet (MV), methyl orange (MO), and methylene blue (MB) as model pollutants under ultraviolet radiation. Analysis of the UV–Vis spectra for the decolorization of these dyes revealed the respective maximum absorption wavelengths (λ_{max}) within the reaction mixture to be 584 nm, 464 nm, and 664 nm, accompanied by a gradual

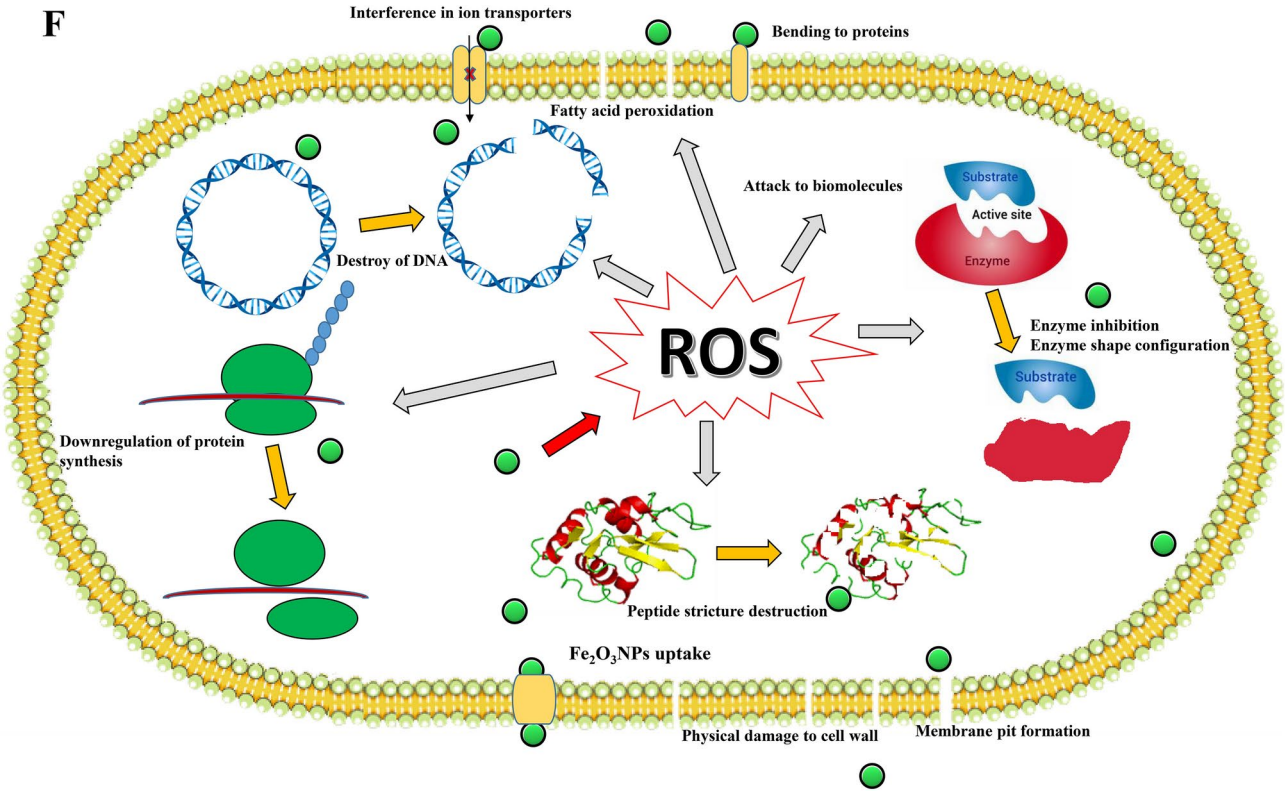

Figure 4. (continued)

decrease in absorption intensity for MV, MO, and MB, respectively (Fig. 6A–C). The presence of Fe_2O_3NPs as a photocatalyst accelerated the degradation of MV, MO, and MB significantly with increasing reaction time, indicating a noticeable trend of color disappearance over time (Fig. 6A-C). The highest rate of dye degradation facilitated by Fe_2O_3NPs was achieved at the end of the experiment (after 1680 min), reaching 89.93%, 84.81%, and 79.71% for MV, MO, and MB, respectively (Fig. 6D). These results highlight the effectiveness of synthesized Fe_2O_3NPs in efficiently eliminating of the evaluated organic dyes from aqueous solutions. Fe_2O_3NPs have demonstrated considerable potential in the degradation of dyes through their photocatalytic activity[70,71]. Upon exposure to light, these nanoparticles generate ROS, notably hydroxyl radicals, which play a pivotal role in oxidizing and breaking down organic dye molecules, thereby facilitating their degradation. Moreover, Fe_2O_3NPs possess the capability to act as both electron acceptors and donors in redox reactions, further augmenting their effectiveness in the degradation of dyes[72]. With their high surface area and reactivity, Fe_2O_3NPs exhibit proficiency in adsorbing dye molecules, thereby enhancing the degradation process. Furthermore, their magnetic properties enable straightforward separation from the reaction mixture post-degradation, promoting their potential for reuse and practical application in the realms of wastewater treatment and environmental remediation. The diverse properties of Fe_2O_3NPs, encompassing photocatalytic activity, redox functionalities, efficient dye adsorption, and magnetic behavior, position them as versatile and potent catalysts in the context of dye degradation processes. This multifaceted nature underscores their promise in advancing environmental sustainability efforts and combating pollution effectively[26,30,73]. The visual representation of the potential mechanism underlying the photocatalytic activity of synthesized Fe_2O_3NPs is depicted in Fig. 6E

Antioxidant assays

The antioxidant potential of the synthesized Fe_2O_3NPs was assessed by means of the DPPH free radical scavenger activity assay. In this assay, the efficacy of the antioxidant in reducing the purple DPPH radical to produce stable yellow DPPH molecules was studied, indicating a hydrogen atom transfer mechanism. Notably, the analysis of variance (ANOVA) revealed a significant antioxidant effect attributable to the Fe_2O_3NPs (Table 4). The Fe_2O_3NPs displayed remarkable antioxidant activity, with a recorded value of 8.45 ± 0.59 μg mL^{-1}, surpassing the performance of ascorbic acid which exhibited an IC_{50} value of 25.19 ± 2.51 μg mL^{-1} (Fig. 7A). The IC50 index analysis clearly indicates that the efficacy of the nanoparticles investigated far surpasses that of ascorbic acid, which is regarded as a standard natural antioxidant. This conclusion is supported by the nanoparticles' capacity to scavenge 50% of DPPH radicals at a significantly lower concentration. This observation implies that distinctive antioxidant components present in the nanoparticles efficiently combat free radicals, such as DPPH, which contain a nitrogen center capable of accepting hydrogen radicals or electrons. Upon reduction of the DPPH radical to its non-radical form, the dark purple DPPH solution underwent a transition to the light purple (Fig. 7B). The absorption associated with this reduction process was measured at 516 nm, indicative of

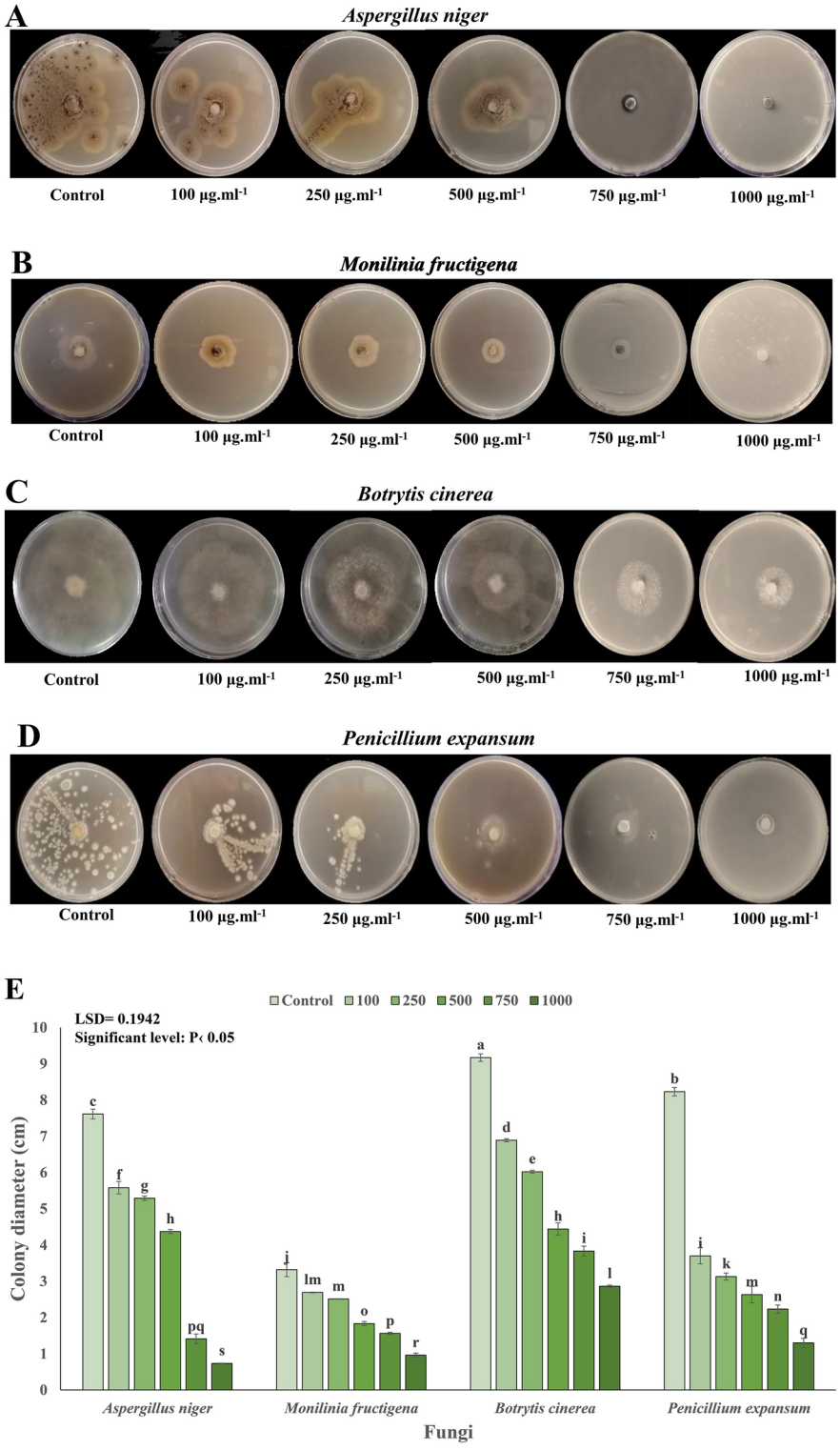

Fig. 5. Antifungal activity of Fe_2O_3NPs against (**A**) *Aspergillus niger*, (**B**) *Monilinia fructigena*, (**C**) *Botrytis cinerea*, (**D**) *Penicillium expansum*; (**E**) Fe_2O_3NPs different concentrations impact on studied fungi; (**F**) Antifungal mechanism of Fe_2O_3NPs.

a robust antioxidant potential[74]. Recent research efforts have extensively explored the antioxidant properties of nanoparticles, particularly focusing on environmentally sustainable variants known for their enhanced antioxidant capabilities[74,75]. The antioxidant activity of nanoparticles relates to their capability to provide hydrogen atoms and unpaired electrons to the medium containing DPPH, thereby effectively neutralizing the

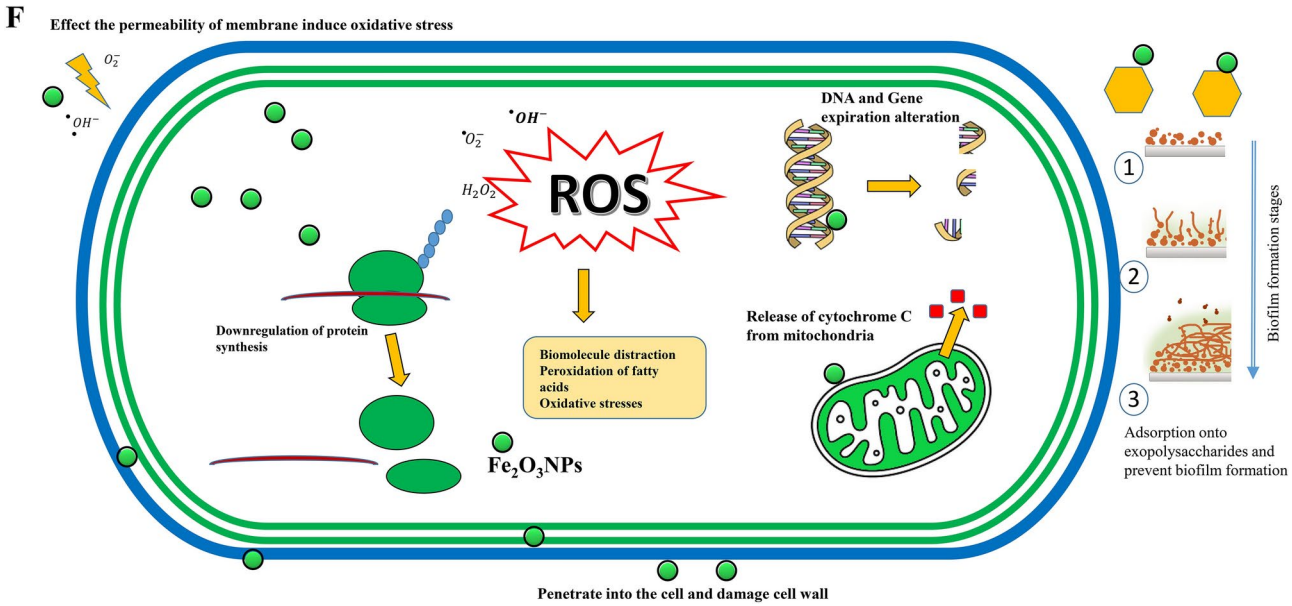

Figure 5. (continued)

target compound[75]. The potential mechanism by which Fe_2O_3NPs exert antioxidant activity is illustrated in Fig. 7C.

Materials and methods

Bacterial solution preparation

The *Pseudomonas fluorescens* was obtained from the microbial repository of the Soil Science Department at Urmia University and was reactivated on solid nutrient agar (NA) medium. Following an incubation period of 48 h, a loopful of the fresh bacterial culture was transferred to an Erlenmeyer flask containing nutrient broth (NB) medium. The flask was agitated on a shaker at 120 rpm for 24 h while being maintained at a temperature of 28 °C.

The bacterial population in the culture medium was quantified by measuring the optical density at 600 nm (OD_{600}), which corresponds to a concentration of 2.01×10^9 bacterial cells per mL of solution[76]. To convert the OD_{600} values into bacterial cell concentrations, the calibration protocol developed by Tennant and Rutten[76] was used[76], which provides guidelines for translating optical density readings into colony-forming units (CFUs). Subsequent to this process, the bacterial suspension was centrifuged at 8000 rpm for 20 min, and the resulting supernatant was utilized for the synthesis of iron nanoparticles.

Iron-nanoparticles biosynthesis

Iron nanoparticles were synthesized using a modified method outlined in prior studies[36,77]. The supernatant of *Pseudomonas fluorescens* bacterial solution, with a volume ratio of 1:1, was combined with an aqueous solution of 0.1 M $FeCl_3.6H_2O$. The resulting mixture was then incubated at 25 °C and stirred at 80 rpm in darkness for 24 h. The change in color of the solution from yellow to dark reddish brown indicated the initiation of iron nanoparticle synthesis[78]. Subsequently, the pH of the sample was adjusted to 7 using 0.1 M sodium hydroxide (NaOH). After 4 h of sonication in a water bath at 80 °C, the samples were washed with 70% ethanol and distilled water (DW) before being dried at 70 °C.

Synthesized iron oxide nanoparticles characteristics

The synthesized Fe_2O_3NPs were thoroughly dried, and a small amount of the sample was mounted on carbon tape and coated with gold through sputtering. Morphological assessment, including the analysis of sizes and structures of these nanoparticles, was conducted using a field- FESEM from ZEISS, the SIGMA VP model manufactured in Germany. This instrument was equipped with EDX sensors from Oxford Instruments, UK, to facilitate detailed compositional analysis[57]. TEM analyses were performed to assess the dimensions, shape, crystalline structure, and dispersion characteristics of the synthesized Fe_2O_3NPs. A drop of the liquid sample solution was placed on the surface of formvar-coated copper grids to prepare the samples for analysis. The specimens were then examined using a TEM device[79], the Philips BioTwin model from the Netherlands, with electron micrographs captured at an accelerating voltage of 75 kV. The dimensions of nanoparticles were ascertained using TEM and SEM imaging with the assistance of Image J software (version ij154), and the resultant histograms were generated using Past 4.03 software.

The crystal structure of Fe_2O_3NPs was investigated using XRD with the X'Pert PRO MRD instrument from PANalytical BV, Netherlands. The nanoparticles were placed on a cavity slide, and a smooth surface was created

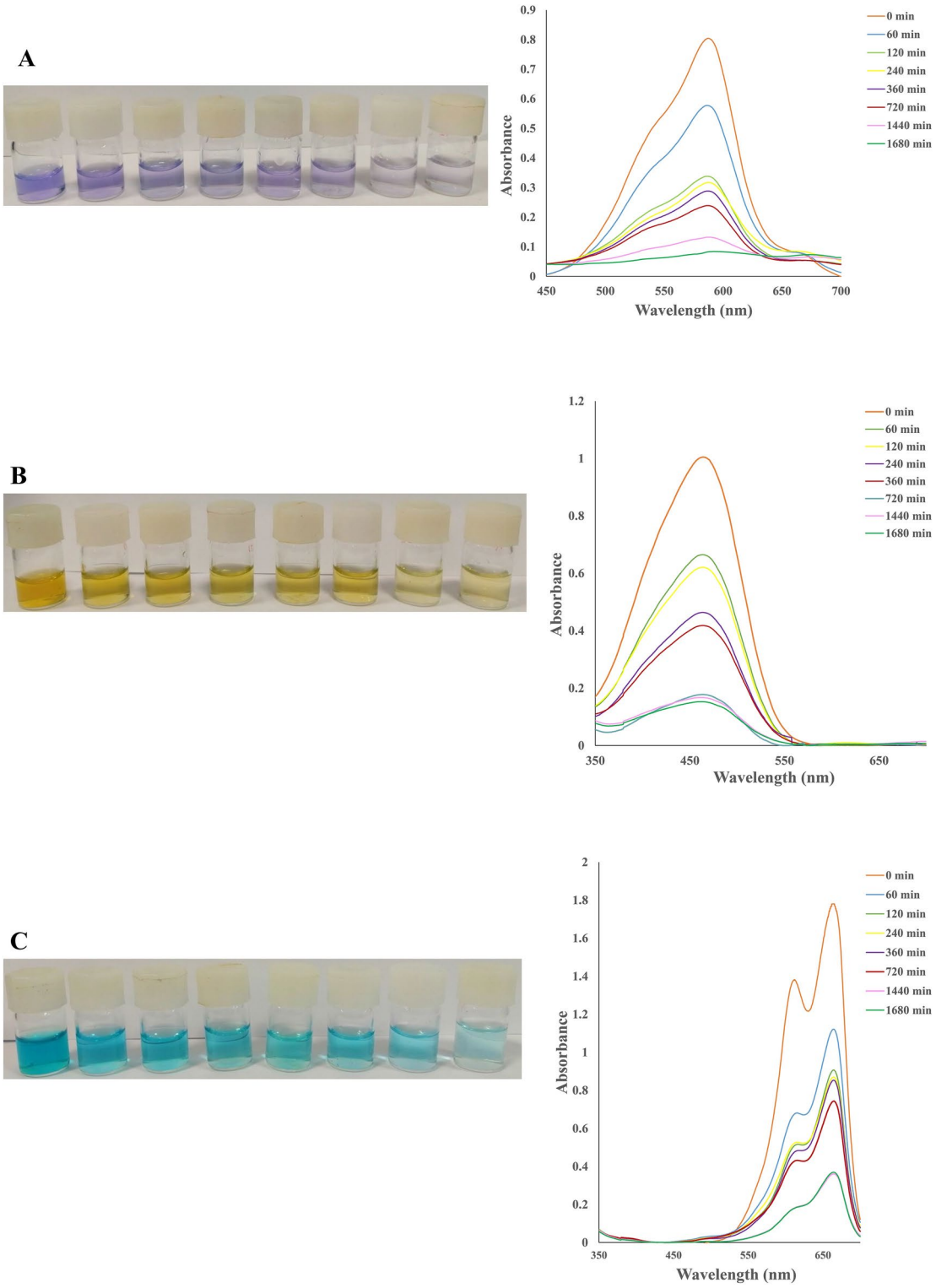

Fig. 6. Photocatalytic activity of Fe_2O_3NPs, color change and UV–vis spectra of (**A**) methyl violet, (**B**) methyl orang, (**C**) methylene blue in different times; (**D**) degradation rate of organic dyes; (**E**) Schematic diagram of Fe_2O_3NPs photocatalytic activity mechanism.

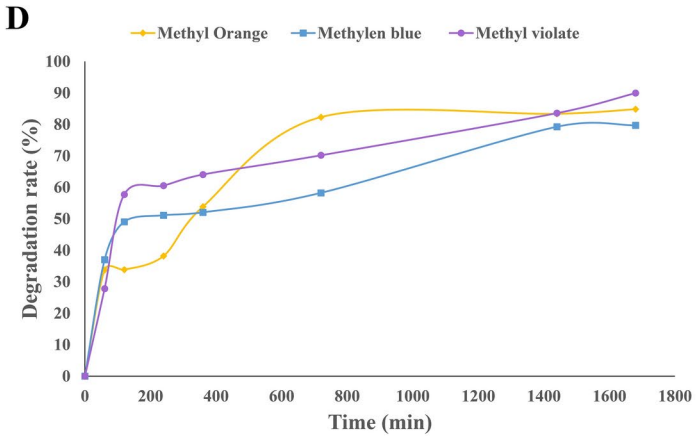

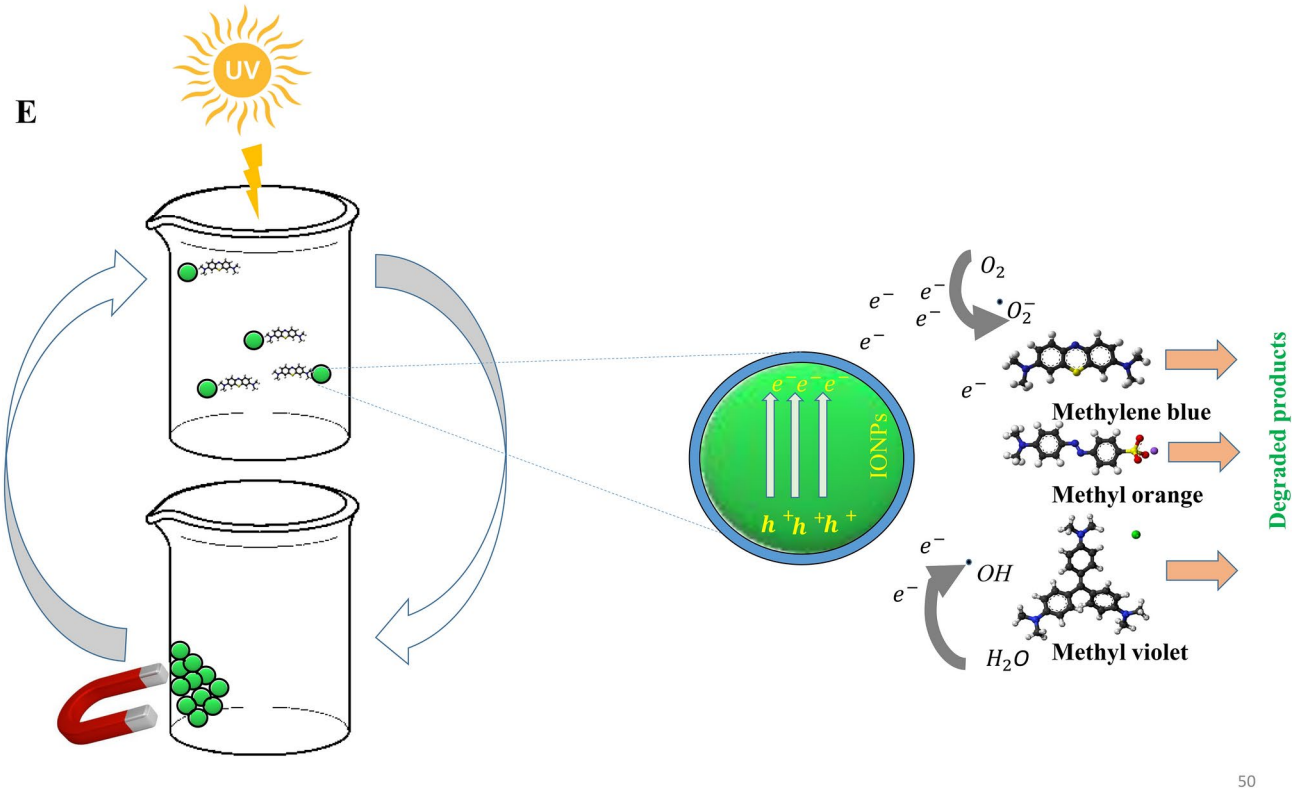

50

Figure 6. (continued)

IC50 DPPH (µg/ml)	df	Mean Square (MS)	F- Value
Treatment	1	420.341***	126.947
Error	4	3.311	
Coefficient of variation (%)		10.82	

Table 4. Analysis of variance (ANOVA) for DPPH IC_{50}. *** represents significance at $P \leq 0.001$.

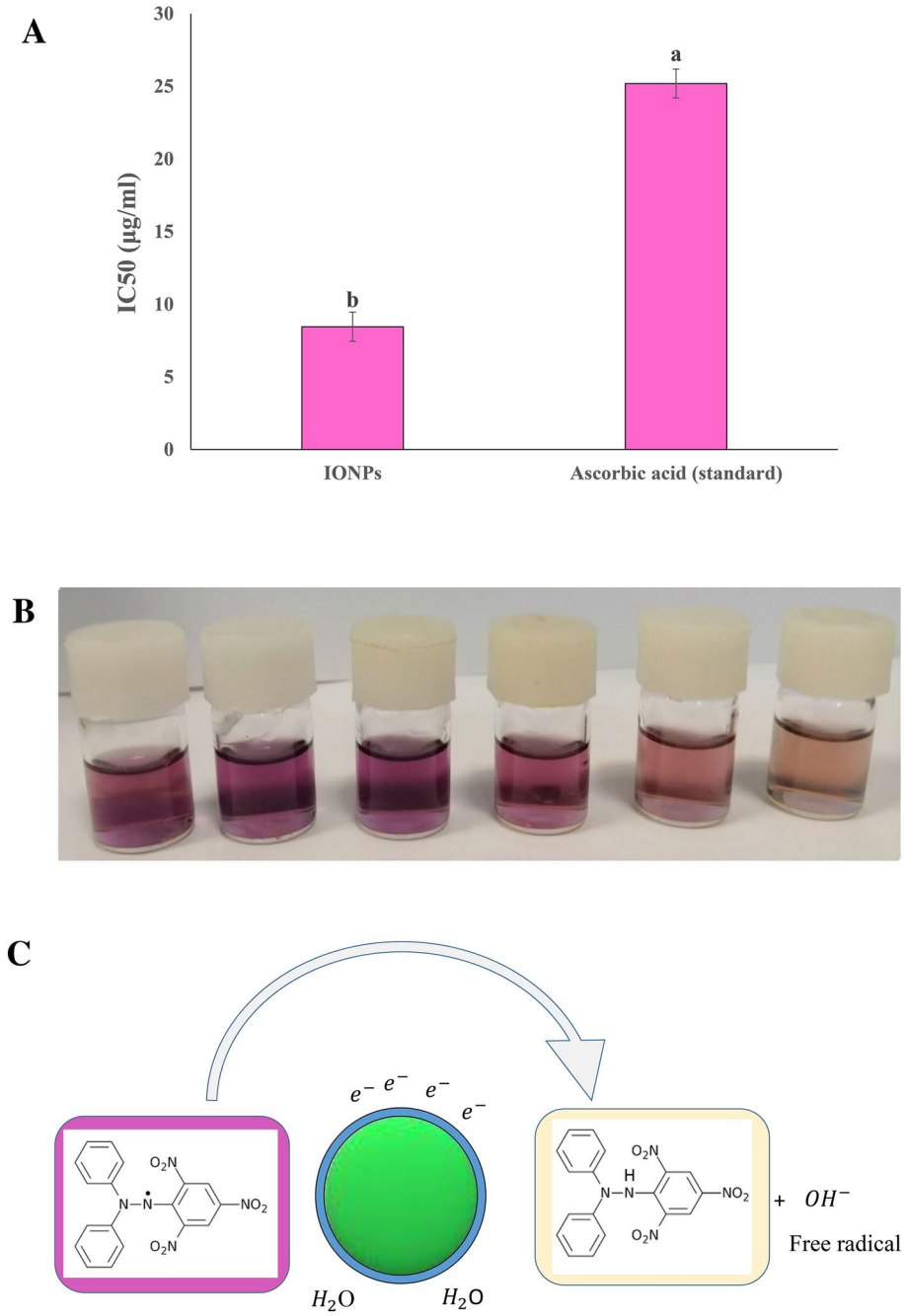

Fig. 7. (**A**) IC_{50} value of Fe_2O_3NPs and ascorbic acid; (**B**) Color change of DPPH in presence of Fe_2O_3NPs different concentrations; (**C**) Schematic diagram of Fe_2O_3NPs antioxidant activity mechanism.

by pressing[65]. XRD measurements were recorded over a 2θ range of 20 to 80 degrees. The crystalline dimensions of the Fe_2O_3NPs were determined using Scherrer's formula (Eq. 1), which is articulated as[80]:

$$D = \frac{K\lambda}{BCos\theta} \tag{1}$$

Here, D signifies the crystal size, K is a constant, λ represents the X-ray wavelength, θ is the diffraction angle, and *B* is a factor associated with the broadening of peaks in the X-ray diffraction pattern.

For the preparation of FTIR samples, Fe_2O_3NPs were first dried in thermostatically controlled desiccators to eliminate any moisture. The dried NPs were then finely crushed and mixed with potassium bromide. This mixture was compacted into a pellet using a hydraulic press[65,81]. The resulting pellets were subsequently analyzed using FTIR spectroscopy with a PerkinElmer Spectrum Two spectrometer from PerkinElmer Instruments, United States. FTIR spectra were recorded by scanning the samples over a wavenumber range of 400 to 4000 cm^{-1} to

identify the functional groups present on the Fe_2O_3NPs. UV–Vis spectroscopy was carried out using a UV–Vis spectrophotometer, specifically the Dynamica HALO DB-20, United Kingdom, encompassing wavelengths from 190 to 700 nm.

The evaluation of surface area and porosity of Fe_2O_3NPs was carried out using BET technique. This assessment was conducted using the Belsorp Mini II instrument, manufactured by BEL JAPAN, INC., located in Hirakata, Japan. Before measuring surface area, samples were degassed in glass cells by heating them in a vacuum for 16 h to eliminate water and contaminants, thereby ensuring the complete removal of unwanted gases. Following the degassing process, the sample cell was transferred to the analysis port and cooled with liquid nitrogen to maintain a low temperature, which is crucial for enhancing interactions between the gas molecules and the sample surface, thus facilitating effective adsorption measurements. Nitrogen gas was then injected into the cell using a calibrated piston. To ensure accuracy, the dead volume of the cell was calibrated before and after each measurement using helium, which does not adsorb onto the sample. Once nitrogen was introduced, the adsorption isotherm was generated, allowing for the calculation of the specific surface area of the sample using the BET equation[82].

The magnetic characteristics of the synthesized particles were evaluated employing a VSM Model LBKFB from Meghnatis Daghigh Kavir Company. Iran, under a magnetic field intensity of 8000 G at room temperature[83].

Antimicrobial assays

Antibacterial activity

Bacteria were obtained from the microbiological bank of the Veterinary Medicine Faculty at Urmia University. The Kirby-Bauer disc diffusion method was employed for investigating the antibacterial effectiveness of synthesized Fe_2O_3NPs against four bacteria, including *Pseudomonas syringae*, *Escherichia coli*, *Salmonella enterica*, and *Staphylococcus aureus*[84]. For the preparation of the growth medium, 28 g of NA were dissolved in 1000 mL of DW and sterilized in an autoclave at 121 °C for 20 min. The sterilized solution was then dispensed into Petri dishes. A bacterial colony was aseptically transferred using a loop, suspended in 10 mL of physiological saline, and adjusted to a half McFarland concentration (OD_{600} = 0.08–0.13). Sterile disks were saturated with varying concentrations (0, 200, 400 µg mL^{-1}) of Fe_2O_3NPs and placed individually on the agar plates inoculated with the bacteria[80]. Subsequently, the plates were incubated at 37 °C for 24 h. The zone of inhibition surrounding the discs, which signifies bacterial growth suppression, was measured using a digital caliper (Carbon model, China). In the experimental setup, the positive control consisted of tetracycline at a concentration of 400 µg mL^{-1}, whereas DW was employed as the negative control.

Antifungal activity

The fungi, including *Aspergillus niger*, *Monilinia fructigena*, *Botrytis cinerea*, and *Penicillium expansum*, were obtained from the microbiological bank of the Plant Protection Department at Urmia University. The antifungal properties of synthesized iron oxide nanoparticles were evaluated using the pour plate method[85]. The experiment was initiated by dissolving 39.1 g of potato dextrose agar (PDA) culture medium in 1000 mL of DW, followed by sterilization at 121 °C for 20 min. After sterilization, the culture medium was divided into six segments, each containing different concentrations of synthesized Fe_2O_3NPs (0 (control), 100, 250, 500, 750, and 1000 µg mL^{-1})[86]. The culture media were thoroughly mixed to ensure uniformity before being dispensed into petri dishes. Once the PDA media had cooled completely, 5-mm loops containing the fungi of interest were carefully placed at the center of the culture medium in the petri dishes. The petri dishes were then placed in a controlled laboratory environment under a hood and incubated for 4 days at room temperature. At the end of the incubation period, the colony diameters of the fungi were precisely measured using a digital caliper (Carbon model, China) to evaluate the impact of the iron oxide nanoparticles on fungal growth.

Dye degradation (Photocatalytic activity)

The previous stablished procedure with a little modification were used for photocatalytic activity[87]. MV, MO, and MB dyes were used for this study. Initially, 0.2 mg of each dye was dissolved in 20 mL of DW, followed by the addition of 10 mg of Fe_2O_3NPs into the dye solution. The resulting mixture underwent exposure to ultraviolet radiation at 30 W while being consistently agitated at 80 rpm. Samples were collected at various time intervals, and the degree of color alteration was assessed as the dye degradation efficiency using Eq. 2[80]. To facilitate this evaluation, UV–vis spectra of the resulting solutions were recorded across the range of 300 to 700 nm. The efficacy of photodegradation and color removal (dye decomposition rate) were determined at the wavelengths corresponding to the peak absorption of MV (584 nm), MO (464 nm), and MB (665 nm), respectively.

$$Degradationrate\,(\%) = \left(\frac{Xc - Xs}{Xs}\right) \times 100 \tag{2}$$

where, Xc and Xs represent the absorbance of MV, MO, or MB in the control and samples containing Fe_2O_3NPs.

Antioxidant properties of synthesized Fe_2O_3NPs

The assessment of the antioxidant activity's IC_{50} was conducted using the DPPH method with slight modifications based on the methodology detailed in a previous study[88]. Initially, a stock solution was prepared by dispersing 120 mg of nanoparticles in 10 mL of DW using a ultrasonic probe dispersion equipment for 5 min. Subsequently, a specific volume ranging from 166 to 500 µL (to achieve concentrations of 2, 3, 4, 5, and 6 mg mL^{-1} of Fe_2O_3NPs) of the prepared composite was transferred into a test tube and subsequently diluted to a final volume of 1 mL

using DW. Following this procedure, 2000 µL of a DPPH solution (0.004 g DPPH dissolved in 100 mL of 80% methanol) was added. The solutions were thoroughly mixed, incubated for 30 min at room temperature, and the absorbance was measured at the wavelength of 516 nm. The DPPH free radical scavenging percentage was calculated using following equation (Eq. 3)[89]:

$$DPPH\,free\,radical\,scavenging\,(\%) = \left(\frac{(Abscontrol - Abssample)}{\text{Abs control}}\right) \times 100 \quad (3)$$

Following this, a graphical representation was constructed plotting the inhibition percentage of DPPH by the samples against the five distinct concentrations. Through the application of linear regression analysis, the IC_{50} values, denoting the concentration at which 50% inhibition was observed, were ascertained. The resultant equation from the analytical process was determined to be $y = 1.9305x + 34.387$, accompanied by an R^2 value of 0.987, signifying a strong correlation between concentration and inhibition percentage.

Statistical analysis

The study experiments were conducted using factorial experiments based on completely randomized designs (CRD). The ANOVA statistical analysis of the data was conducted using the MSTAT-C software (version 4.1), with means comparison being executed through the Duncan's multiple comparison test. Graphs were generated using Excel 2016 software.

Conclusion

Pseudomonas fluorescens has demonstrated promising capabilities for the extracellular synthesis of Fe_2O_3NPs. Multiple analytical techniques, including UV–Vis spectroscopy, XRD, FTIR, SEM, EDX, TEM, BET, and VSM analytical techniques were utilized to validate the characteristics of the nanoparticles. Examination through TEM revealed a spherical morphology, with the particle dimensions falling within the range of 7 to 37 nm. The mesoporous Fe_2O_3NPs exhibited a specific surface area of 271.4 $m^2\ g^{-1}$, an average pore diameter of 2.47 nm, and a BJH pore volume of 0.0952 $cm^3\ g^{-1}$ as determined by BET method. Additionally, the mean particle size, as assessed by XRD analysis, was calculated to be 22.73 nm. The assessment of the synthesized Fe_2O_3NPs demonstrated significant multifunctional properties, including antimicrobial, photocatalytic, and antioxidant activities. The Fe_2O_3NPs demonstrated potent inhibition of bacterial growth, with maximum inhibition zones ranging from 7.25 ± 0.102 mm to 8.35 ± 0.103 mm observed in key bacterial strains, including *S. aureus*, *E. coli*, *S. enterica*, and *P. syringae*, at a concentration of 400 µg mL^{-1}. In the assessment of antifungal activity, the Fe_2O_3NPs exhibited inhibitory effects on the growth of all tested fungi across a concentration range of 100 to 1000 µg mL^{-1}. With escalating concentrations of Fe_2O_3NPs, the suppressive effect of the nanoparticles intensified correspondingly. The smallest colony diameters recorded in *A. niger*, *M. fructigena*, *B. cinerea*, and *P. expansum* were 0.73 ± 0.01 cm, 0.96 ± 0.05 cm, 2.86 ± 0.03 cm, and 1.3 ± 0.12 cm, respectively, at the highest concentration (1000 µg mL^{-1}) of the synthesized nanoparticles. A significant aspect of these findings is that the nature of the produced nanoparticles suggests their potential application on solid surfaces in the textile and food packaging industries. Such applications could create sterile conditions and effectively inhibit the growth of bacteria and fungi. The findings revealed that Fe_2O_3NPs exhibited degradation efficiencies surpassing 89.93%, 84.81%, and 79.71% against MV, MO, and MB, respectively. The notable photocatalytic efficacy of these iron nanoparticles against three prominent industrial dyes highlights their substantial potential, thereby necessitating in-depth exploration for potential practical applications. Moreover, the assessment of antioxidant activity demonstrated that Fe_2O_3NPs displayed a scavenging capacity of 50% towards the initial DPPH radicals at a concentration of 8.45 ± 0.59 µg mL^{-1}, outperforming the antioxidant efficacy of ascorbic acid, which exhibited an IC_{50} value of 25.19 ± 2.51 µg mL^{-1}. Iron oxide nanoparticles, particularly those that are environmentally friendly, hold significant potential for transforming various sectors through their versatile applications. They offer a range of advantages and show promise in addressing environmental contaminants and advancing healthcare and pharmaceutical fields. Understanding the biochemical and molecular mechanisms behind nanoparticle synthesis using cell-free supernatants of microorganisms is essential for achieving precise control over nanoparticle size. Further research is needed to enhance our knowledge and broaden the applications of these nanoparticles by refining synthesis processes and ensuring in-depth characterization. Standardized protocols for different methodologies are necessary to maximize nanoparticle efficacy. Furthermore, investigating the potential impacts of these nanoparticles on soil ecosystems and human health is crucial for ensuring their safe and sustainable deployment across industries to promote improved environmental stewardship.

Data availability

Upon request, the data will be made accessible. Contact with Corresponding authors.

Received: 22 September 2024; Accepted: 30 December 2024
Published online: 06 January 2025

References

1. Khan, I., Saeed, K. & Khan, I. Nanoparticles: Properties, applications and toxicities. *Arab. J. Chem.* **12**, 908–931. https://doi.org/10.1016/j.arabjc.2017.05.011 (2019).
2. Govindaraju, K., Tamilselvan, S., Kiruthiga, V., Singaravelu, G. (2010). Biogenic silver nanoparticles by *Solanum torvum* and their promising antimicrobial activity. J Biopestic. 3, 394.
3. Ijaz, I., Gilani, E., Nazir, A. & Bukhari, A. Detail review on chemical, physical and green synthesis, classification, characterizations and applications of nanoparticles. *Green chem. lett. rev.* **13**, 223–245. https://doi.org/10.1080/17518253.2020.1802517 (2020).

4. Srivastava, S. et al. Biological nanofactories: Using living forms for metal nanoparticle synthesis. *Mini-Rev. Med. Chem.* **21**, 245–265. https://doi.org/10.2174/1389557520999201116163012 (2021).
5. Din, M. I., Nabi, A. G., Rani, A., Aihetasham, A. & Mukhtar, M. Single step green synthesis of stable nickel and nickel oxide nanoparticles from Calotropis gigantea: catalytic and antimicrobial potentials. *Environ. Nanotechnol. Monit. Manag.* **9**, 29–36. https://doi.org/10.1016/j.enmm.2017.11.005 (2018).
6. Taib, N. I., Latif, F. A., Mohamed, Z. & Zambri, N. S. (2018). Green synthesis of iron oxide nanoparticles (Fe3O4-NPs) using *Azadirachta indica* aqueous leaf extract. Int. J. Eng. Technol 7, 9–13. https://doi.org/10.14419/ijet.v7i4.18.21811
7. Priya, Naveen, Kaur, K. & Sidhu, A. K. Green synthesis: An eco-friendly route for the synthesis of iron oxide nanoparticles. Front. Nanotechnol. 3, 655062. https://doi.org/10.3389/fnano.2021.655062 (2021).
8. Ying, S. et al. Green synthesis of nanoparticles: Current developments and limitations. *Environ. Technol. Innov.* **26**, 102336. https://doi.org/10.1016/j.eti.2022.102336 (2022).
9. Ali, M. A. et al. Advancements in plant and microbe-based synthesis of metallic nanoparticles and their antimicrobial activity against plant pathogens. *Nanomaterials* **10**, 1146. https://doi.org/10.3390/nano10061146 (2020).
10. Khan, T., Abbas, S., Fariq, A. & Yasmin, A. Microbes: Nature's cell factories of nanoparticles synthesis. Exp. Realms Nat Nanosynth., 25–50. https://doi.org/10.1007/978-3-319-99570-0_2 (2018).
11. Mohd Yusof, H., Mohamad, R., Zaidan, U. H. & Abdul Rahman, N. A. Microbial synthesis of zinc oxide nanoparticles and their potential application as an antimicrobial agent and a feed supplement in animal industry: a review. J. Anim. Sci. Biotechnol. 10, 1–22. https://doi.org/10.1186/s40104-019-0368-z (2019).
12. Hulkoti, N. I. & Taranath, T. Biosynthesis of nanoparticles using microbes—a review. *Colloid Surf. B-Biointerfaces.* **121**, 474–483. https://doi.org/10.1016/j.colsurfb.2014.05.027 (2014).
13. Jain, N., Bhargava, A., Majumdar, S., Tarafdar, J. & Panwar, J. Extracellular biosynthesis and characterization of silver nanoparticles using Aspergillus flavus NJP08: a mechanism perspective. *Nanoscale* **3**, 635–641. https://doi.org/10.1039/C0NR00656D (2011).
14. Khand, N. H. et al. in Nanomaterials in Biomass Conversion 85–116 (Elsevier, 2024).
15. Bahrulolum, H. et al. Green synthesis of metal nanoparticles using microorganisms and their application in the agrifood sector. *J. Nanobiotechnol.* **19**, 1–26. https://doi.org/10.1186/s12951-021-00834-3 (2021).
16. Syed, B., Prasad, N., Dhananjaya, B., Yallappa, S. & Satish, S. Synthesis of silver nanoparticles by endosymbiont Pseudomonas fluorescens CA 417 and their bactericidal activity. *Enzyme Microb. Technol.* **95**, 128–136. https://doi.org/10.1016/j.enzmictec.2016.10.004 (2016).
17. Singh, B., Garg, T., Goyal, A. K. & Rath, G. Development, optimization, and characterization of polymeric electrospun nanofiber: a new attempt in sublingual delivery of nicorandil for the management of angina pectoris. *Artif. cells nanomed. biotechnol.* **44**, 1498–1507. https://doi.org/10.3109/21691401.2015.1052472 (2016).
18. Corr, S. A. Metal oxide nanoparticles. *Nanoscience* **1**, 180–207 (2012).
19. Tran, N. et al. (2010). Bactericidal effect of iron oxide nanoparticles on Staphylococcus aureus. Int. J. Nanomed. https://doi.org/10.2147/IJN.S9220
20. Pereira, L. & Alves, M. Dyes—environmental impact and remediation. Environmental protection strategies for sustainable development. https://doi.org/10.1007/978-94-007-1591-2_4 (2012).
21. Iyyappan, J. et al. Critical review on wastewater treatment using photo catalytic advanced oxidation process: Role of photocatalytic materials, reactor design and kinetics. Case Stud. Chem. Environ. Eng. https://doi.org/10.1016/j.cscee.2023.100599 (2023).
22. Tahir, M. B., Sohaib, M., Sagir, M. & Rafique, M. Role of nanotechnology in photocatalysis. Encyclopedia of smart materials. https://doi.org/10.1016/B978-0-12-815732-9.00006-1 (2022).
23. Aragaw, T. A., Bogale, F. M. & Aragaw, B. A. Iron-based nanoparticles in wastewater treatment: A review on synthesis methods, applications, and removal mechanisms. *J. Saudi Chem. Soc.* **25**, 101280. https://doi.org/10.1016/j.jscs.2021.101280 (2021).
24. Nadeem, M. et al. A review of microbial mediated iron nanoparticles (IONPs) and its biomedical applications. *Nanomaterials* **12**, 130. https://doi.org/10.3390/nano12010130 (2021).
25. Razack, S. A. et al. Green synthesis of iron oxide nanoparticles using Hibiscus rosa-sinensis for fortifying wheat biscuits. *SN Appl. Sci.* **2**, 1–9. https://doi.org/10.1007/s42452-020-2477-x (2020).
26. Suppiah, D. D., Julkapli, N. M., Sagadevan, S. & Johan, M. R. Eco-friendly green synthesis approach and evaluation of environmental and biological applications of Iron oxide nanoparticles. *Inorg. Chem. Commun.* **152**, 110700. https://doi.org/10.1016/j.inoche.2023.110700 (2023).
27. Hoseinzadeh, E. et al. A review on nano-antimicrobials: metal nanoparticles, methods and mechanisms. *Curr. Drug Metab.* **18**, 120–128. https://doi.org/10.2174/1389200217666161201111146 (2017).
28. Slavin, Y. N. & Bach, H. Mechanisms of antifungal properties of metal nanoparticles. *Nanomaterials* **12**, 4470. https://doi.org/10.3390/nano12244470 (2022).
29. Krishna, P. G. et al. Photocatalytic activity induced by metal nanoparticles synthesized by sustainable approaches: a comprehensive review. *Front. Chem.* **10**, 917831. https://doi.org/10.3389/fchem.2022.917831 (2022).
30. Kumar, B. Green synthesis of gold, silver, and iron nanoparticles for the degradation of organic pollutants in wastewater. *J. Compos. Sci.* **5**, 219. https://doi.org/10.3390/jcs5080219 (2021).
31. Samrot, A. V. et al. Nanoparticles, a double-edged sword with oxidant as well as antioxidant properties—a review. *Oxygen* **2**, 591–604. https://doi.org/10.3390/oxygen2040039 (2022).
32. Moghaddam, K. An introduction to microbial metal nanoparticle preparation method. J. Young Investig. (2010).
33. Sangeeta, M. et al. In-vitro evaluation of Talaromyces islandicus mediated zinc oxide nanoparticles for antibacterial, anti-inflammatory, bio-pesticidal and seed growth promoting activities. *Waste Biomass Valorization* **15**, 1901–1915. https://doi.org/10.1007/s12649-023-02386-z (2024).
34. Wei, Y., Han, S., Walker, D. A., Warren, S. C. & Grzybowski, B. A. Enhanced photocatalytic activity of hybrid Fe2O3–Pd nanoparticulate catalysts. *Chem. Sci.* **3**, 1090–1094. https://doi.org/10.1039/C2SC00673A (2012).
35. Sandler, S. E., Fellows, B. & Mefford, O. T. (ACS Publications, 2019).
36. Minhas, L. A. et al. Biogenic fabrication of iron oxide nanoparticles from Leptolyngbya sp. L-2 and multiple in vitro pharmacogenetic properties. Toxics 11, 561. https://doi.org/10.3390/toxics11070561 (2023).
37. Sasani, M., Fataei, E., Safari, R., Nasehi, F. & Mosayebi, M. Antibacterial effects of iron oxide and silver nanoparticles synthesized by Bacillus subtilis: a comparative study. *Desalination Water Treat* **231**, 340–347. https://doi.org/10.5004/dwt.2021.27498 (2021).
38. Mondal, P., Anweshan, A. & Purkait, M. K. Green synthesis and environmental application of iron-based nanomaterials and nanocomposite: A review. *Chemosphere* **259**, 127509. https://doi.org/10.1016/j.chemosphere.2020.127509 (2020).
39. Xu, W. et al. Insights into the Synthesis, types and application of iron Nanoparticles: The overlooked significance of environmental effects. *Environ. Int.* **158**, 106980. https://doi.org/10.1016/j.envint.2021.106980 (2022).
40. Nayaka, S. et al. Biosynthesis, characterization, and in vitro assessment on cytotoxicity of actinomycete-synthesized silver nanoparticles on Allium cepa root tip cells. *Beni-Suef Univ. J. Basic Appl. Sci.* **9**, 1–18. https://doi.org/10.1186/s43088-020-00074-8 (2020).
41. Khan, S. et al. Biosynthesized iron oxide nanoparticles (Fe3O4NPs) mitigate arsenic toxicity in rice seedlings. *Toxics* **9**, 2. https://doi.org/10.3390/toxics9010002 (2020).
42. Syarif, N., Tribidasari, A. & Wibowo, W. Direct synthesis carbon/Metal oxide composites for electrochemical capacitors electrode. Int. Trans. J. Eng. Manag. Appl. Sci. Technol. 3, 21–34. (2012).

43. Siddhardha Busi, S. B., Jobina Rajkumari, J. R., Subhaswaraj Pattnaik, S. P., Paramanandham Parasuraman, P. P. & Sairengpuii Hnamte, S. H. Extracellular synthesis of zinc oxide nanoparticles using Acinetobacter schindleri SIZ7 and its antimicrobial property against foodborne pathogens. J. Microbiol. Biotechnol. Food Sci. 5, 407. https://doi.org/10.15414/jmbfs.2016.5.5.407-411 (2016).
44. Feng, B. et al. Synthesis of Fe3O4/APTES/PEG diacid functionalized magnetic nanoparticles for MR imaging. *Colloid Surf. A-Physicochem. Eng. Asp.* **328**, 52–59. https://doi.org/10.1016/j.colsurfa.2008.06.024 (2008).
45. Devatha, C., Thalla, A. K. & Katte, S. Y. Green synthesis of iron nanoparticles using different leaf extracts for treatment of domestic waste water. *Clean. Prod.* **139**, 1425–1435. https://doi.org/10.1016/j.jclepro.2016.09.019 (2016).
46. Kanagasubbulakshmi, S. & Kadirvelu, K. Green synthesis of iron oxide nanoparticles using Lagenaria siceraria and evaluation of its antimicrobial activity. Def. Life Sci. J. 2, 422–427. https://doi.org/10.14429/dlsj.2.12277 (2017).
47. Arjaghi, S. K., Alasl, M. K., Sajjadi, N., Fataei, E. & Rajaei, G. E. Retracted article: green synthesis of Iron oxide nanoparticles by RS Lichen extract and its application in removing heavy metals of lead and cadmium. *Biol. Trace Elem. Res.* **199**, 763–768. https://doi.org/10.1007/s12011-020-02170-3 (2021).
48. Luque, R., Gawande, M. B., Doustkhah, E. & Goswami, A. Solvent-free Methods in Nanocatalysis: From Catalyst Design to Applications. (John Wiley & Sons, 2023).
49. Agrawal, M. et al. in E3S Web of Conferences. 01029 (EDP Sciences, 2024).
50. Sing, K. S. Reporting physisorption data for gas/solid systems with special reference to the determination of surface area and porosity (Recommendations 1984). *Pure Appl. Chem.* **57**, 603–619. https://doi.org/10.1351/pac198557040603 (1985).
51. Abolhasani Zadeh, F. et al. Drug delivery and anticancer activity of biosynthesised mesoporous Fe2O3 nanoparticles. IET Nanobiotechnol. 16, 85–91. https://doi.org/10.1049/nbt2.12080 (2022).
52. Jiao, K. et al. The characterization and quantitative analysis of nanopores in unconventional gas reservoirs utilizing FESEM–FIB and image processing: An example from the lower Silurian Longmaxi Shale, upper Yangtze region. *China. Int. J. Coal Geol.* **128**, 1–11. https://doi.org/10.1016/j.coal.2014.03.004 (2014).
53. Taulo, S., Wetlesen, A., Abrahamsen, R., Narvhus, J. & Mkakosya, R. Quantification and variability of Escherichia coli and Staphylococcus aureus cross-contamination during serving and consumption of cooked thick porridge in Lungwena rural households. *Malawi. Food Control* **20**, 1158–1166. https://doi.org/10.1016/j.foodcont.2009.03.009 (2009).
54. Grudlewska-Buda, K. et al. Antibiotic Resistance in selected emerging bacterial foodborne Pathogens—An issue of concern?. *Antibiotics* **12**, 880. https://doi.org/10.3390/antibiotics12050880 (2023).
55. Liang, T. et al. Simultaneous detection of viable Salmonella spp., Escherichia coli, and Staphylococcus aureus in bird's nest, donkey-hide gelatin, and wolfberry using PMA with multiplex real-time quantitative PCR. Food Sci. Nutr. 10, 3165–3174. https://doi.org/10.1002/fsn3.2916 (2022).
56. Morris, C. E. et al. The life history of the plant pathogen Pseudomonas syringae is linked to the water cycle. *ISME J.* **2**, 321–334. https://doi.org/10.1038/ismej.2007.113 (2008).
57. Shashiraj, K. N. et al. Exploring the antimicrobial, anticancer, and apoptosis inducing ability of biofabricated silver nanoparticles using Lagerstroemia speciosa flower buds against the Human Osteosarcoma (MG-63) cell line via flow cytometry. *Bioengineering* **10**, 821. https://doi.org/10.3390/bioengineering10070821 (2023).
58. Bhat, M. P. et al. Aspergillus niger CJ6 extract with antimicrobial potential promotes in-vitro cytotoxicity and induced apoptosis against MIA PaCa-2 cell line. *Environ. Res.* **229**, 116008. https://doi.org/10.1016/j.envres.2023.116008 (2023).
59. Radini, I. A., Hasan, N., Malik, M. A. & Khan, Z. Biosynthesis of iron nanoparticles using Trigonella foenum-graecum seed extract for photocatalytic methyl orange dye degradation and antibacterial applications. *J. Photochem. Photobiol. B.* **183**, 154–163. https://doi.org/10.1016/j.jphotobiol.2018.04.014 (2018).
60. Yamamoto, O., Sawai, J. & Sasamoto, T. Change in antibacterial characteristics with doping amount of ZnO in MgO–ZnO solid solution. *Int. J. Inorg. Mater.* **2**, 451–454. https://doi.org/10.1016/S1466-6049(00)00045-3 (2000).
61. Kadiyala, U., Kotov, N. A. & VanEpps, J. S. Antibacterial metal oxide nanoparticles: challenges in interpreting the literature. *Curr. Pharm. Des.* **24**, 896–903. https://doi.org/10.2174/1381612824666180219130659 (2018).
62. Nikolova, M. P. & Chavali, M. S. Metal oxide nanoparticles as biomedical materials. *Biomimetics* **5**, 27. https://doi.org/10.3390/biomimetics5020027 (2020).
63. Math, H. H. et al. Investigation of in vitro anticancer and apoptotic potential of biofabricated silver nanoparticles from *Cardamine hirsuta* (L.) leaf extract against Caco-2 cell line. Inorganics 11, 322. https://doi.org/10.3390/inorganics11080322 (2023).
64. Bhat, M. et al. Biogenic synthesis, characterization and antimicrobial activity of Ixora brachypoda (DC) leaf extract mediated silver nanoparticles. *J. King Saud Univ. Sci.* **33**, 101296. https://doi.org/10.1016/j.jksus.2020.101296 (2021).
65. Rudrappa, M. et al. Myco-nanofabrication of silver nanoparticles by Penicillium brasilianum NP5 and their antimicrobial, photoprotective and anticancer effect on MDA-MB-231 breast cancer cell line. *Antibiotics* **12**, 567. https://doi.org/10.3390/antibiotics12030567 (2023).
66. Shashiraj, K. N. et al. Rotheca serrata flower bud extract mediated bio-friendly preparation of silver nanoparticles: Their characterizations, anticancer, and apoptosis inducing ability against pancreatic ductal adenocarcinoma cell line. *Processes* **11**, 893. https://doi.org/10.3390/pr11030893 (2023).
67. Bento de Carvalho, T., Silva, B. N., Tomé, E. & Teixeira, P. Preventing fungal spoilage from raw materials to final product: Innovative preservation techniques for fruit fillings. Foods 13, 2669. (2024).
68. Mari, M., Martini, C., Guidarelli, M. & Neri, F. Postharvest biocontrol of Monilinia laxa, Monilinia fructicola and Monilinia fructigena on stone fruit by two Aureobasidium pullulans strains. *Biol. Control* **60**, 132–140. https://doi.org/10.1016/j.biocontrol.2011.10.013 (2012).
69. Devi, H. S., Boda, M. A., Shah, M. A., Parveen, S. & Wani, A. H. Green synthesis of iron oxide nanoparticles using Platanus orientalis leaf extract for antifungal activity. *Green Process. Synth.* **8**, 38–45. https://doi.org/10.1515/gps-2017-0145 (2019).
70. Carmona-Carmona, A. J. et al. Photocatalytic Degradation of Methylene Blue by Magnetic Opal/Fe3O4 Colloidal Crystals under Visible Light Irradiation. *Photochem* **3**, 390–407. https://doi.org/10.3390/photochem3040024 (2023).
71. Kaushik, J. et al. Photoactive Fe3O4@ Fe2O3 Synthesized from Industrial Iron Oxide Dust for Fenton-Free Degradation of Multiple Organic Dyes. *Ind. Eng. Chem. Res.* **62**, 10487–10497. https://doi.org/10.1021/acs.iecr.3c01098 (2023).
72. Lanjwani, M. F., Tuzen, M., Khuhawar, M. Y. & Saleh, T. A. Trends in photocatalytic degradation of organic dye pollutants using nanoparticles: a review. *Inorg. Chem. Commun.* **159**, 111613. https://doi.org/10.1016/j.inoche.2023.111613 (2024).
73. Albeladi, A. et al. Fe3O4-CdO nanocomposite for organic dye photocatalytic degradation: synthesis and characterization. *Catal.* **14**, 71. https://doi.org/10.3390/catal14010071 (2024).
74. Perveen, S. et al. Green synthesis of iron (Fe) nanoparticles using Plumeria obtusa extract as a reducing and stabilizing agent: antimicrobial, antioxidant and biocompatibility studies. *Arab. J. Chem.* **15**, 103764. https://doi.org/10.1016/j.arabjc.2022 (2022).
75. Majeed, S. et al. Bacteria mediated synthesis of iron oxide nanoparticles and their antibacterial, antioxidant, cytocompatibility properties. *J. Clust. Sci.* **32**, 1083–1094. https://doi.org/10.1007/s10876-020-01876-7 (2021).
76. Tennant, R. & Rutten, P. Calibration Protocol-Conversion of OD to Colony Forming Units (CFUs). https://doi.org/10.17504/protocols.io.zgnf3ve (2019).
77. Jubran, A. S., Al-Zamely, O. M. & Al-Ammar, M. H. A study of iron oxide nanoparticles synthesis by using bacteria. Int. J. Pharm. Qual. Assur. 11, 01–08. https://doi.org/10.25258/ijpqa.11.1.13 (2020).

78. Fatemi, M., Mollania, N., Momeni-Moghaddam, M. & Sadeghifar, F. Extracellular biosynthesis of magnetic iron oxide nanoparticles by Bacillus cereus strain HMH1: characterization and in vitro cytotoxicity analysis on MCF-7 and 3T3 cell lines. *J. Biotechnol.* **270**, 1–11. https://doi.org/10.1016/j.jbiotec.2018.01.021 (2018).
79. Kong, L. et al. Facile hermetic TEM grid preparation for molecular imaging of hydrated biological samples at room temperature. *Nat. Commun.* **14**, 5641. https://doi.org/10.1038/s41467-023-41266-x (2023).
80. Yousefzadeh-Valendeh, S., Fattahi, M., Asghari, B. & Alizadeh, Z. Dandelion flower-fabricated Ag nanoparticles versus synthetic ones with characterization and determination of photocatalytic, antioxidant, antibacterial, and α-glucosidase inhibitory activities. *Sci Rep* **13**, 15444. https://doi.org/10.1038/s41598-023-42756-0 (2023).
81. Stoia, M., Istratie, R. & Păcurariu, C. Investigation of magnetite nanoparticles stability in air by thermal analysis and FTIR spectroscopy. *J. Therm. Anal. Calorim.* **125**, 1185–1198. https://doi.org/10.1007/s10973-016-5393-y (2016).
82. Raja, P. M. & Barron, A. R. BET surface area analysis of nanoparticles. Rice University (2021).
83. Kirupakar, B., Vishwanath, B., Sree, M. P. & Deenadayalan, D. Vibrating sample magnetometer and its application in characterization of magnetic property of the anticancer drug magnetic microspheres. Int. J. Pharm. Drug. Anal. 4, 227–233. (2016).
84. Harshiny, M., Iswarya, C. N. & Matheswaran, M. Biogenic synthesis of iron nanoparticles using *Amaranthus dubius* leaf extract as a reducing agent. *Powder Technol.* **286**, 744–749. https://doi.org/10.1016/j.powtec.2015.09.021 (2015).
85. Iranbakhsh, A., Ebadi, M. & Bayat, M. The inhibitory effects of plant methanolic extract of Datura stramonium L. and leaf explant callus against bacteria and fungi. Glob. Vet. 4, 149–155. (2010).
86. Parveen, S. et al. Preparation, characterization and antifungal activity of iron oxide nanoparticles. *Microb. Pathog.* **115**, 287–292. https://doi.org/10.1016/j.micpath.2017.12.068 (2018).
87. Jiang, W. et al. Silver oxide as superb and stable photocatalyst under visible and near-infrared light irradiation and its photocatalytic mechanism. *Ind. Eng. Chem. Res.* **54**, 832–841. https://doi.org/10.1021/ie503241k (2015).
88. Alizadeh, Z. & Fattahi, M. Essential oil, total phenolic, flavonoids, anthocyanins, carotenoids and antioxidant activity of cultivated Damask Rose (Rosa damascena) from Iran: With chemotyping approach concerning morphology and composition. *Sci. Hortic.* **288**, 110341. https://doi.org/10.1016/j.scienta.2021.110341 (2021).
89. Mohammadi, E., Fattahi, M., Barin, M. & Ashrafi-Saeidlou, S. Arbuscular mycorrhiza and vermicompost alleviate drought stress and enhance yield, total flavonoid concentration, rutin content, and antioxidant activity of buckwheat (Fagopyrum esculentum Moench). *S. Afr. J. Bot.* **148**, 588–600. https://doi.org/10.1016/j.sajb.2022.05.020 (2022).

Acknowledgements

The authors extend their appreciation to the Soil Science and Horticulture Departments of Urmia University for their valuable assistance in the execution of this study. Furthermore, the Electron Microscope Center of Urmia University is acknowledged for facilitating access to the TEM facility.

Author contributions

Sanaz Ashrafi-Saiedlou: Writing—original draft, Writing- review and editing, Investigation, Data curation, Software, Methodology. MirHassan Rasouli-Sadaghiani: Conceptualization, Project administration, Supervision. Mohammad Fattahi: Supervision, Conceptualization, Project administration, Methodology. Youbert Ghosta: Conceptualization, Methodology.

Funding

Funding for this study was not received from any public, commercial, or non-profit sources.

Declarations

Conflict of interest

The authors declare no competing interests.

Additional information

Correspondence and requests for materials should be addressed to S.A.-S. or M.R.-S.